SPACE SCIENCES

Paleomagnetic evidence for a disk substructure in the early solar system

Cauê S. Borlina[1]*, Benjamin P. Weiss[1], James F. J. Bryson[2], Xue-Ning Bai[3], Eduardo A. Lima[1], Nilanjan Chatterjee[1], Elias N. Mansbach[1]

Astronomical observations and isotopic measurements of meteorites suggest that substructures are common in protoplanetary disks and may even have existed in the solar nebula. Here, we conduct paleomagnetic measurements of chondrules in CO carbonaceous chondrites to investigate the existence and nature of these disk substructures. We show that the paleomagnetism of chondrules in CO carbonaceous chondrites indicates the presence of a 101 ± 48 μT field in the solar nebula in the outer solar system (~3 to 7 AU from the Sun). The high intensity of this field relative to that inferred from inner solar system (~<3 AU) meteorites indicates a factor of ~5 to 150 mismatch in nebular accretion between the two reservoirs. This suggests substantial mass loss from the disk associated with a major disk substructure, possibly due to a magnetized disk wind.

INTRODUCTION

Observations from the Atacama Large Millimeter/submillimeter Array have shown that substructures, mostly in the form of rings and gaps, are prevalent in protoplanetary disks (*1*). Isotopic studies of meteorites and their components have been interpreted as evidence that two isotopically distinct regions existed within ~7 astronomical units (AU) from the young Sun (see the Supplementary Materials), known as the noncarbonaceous (<3 AU) and carbonaceous reservoirs (3 to 7 AU) (*2*, *3*), that existed during the protoplanetary disk phase of the solar system (i.e., solar nebula). It has been proposed that these two reservoirs were separated by a gap in the disk, perhaps generated by the growth of Jupiter (*4*) and/or a pressure local maximum in the disk (*5*). Alternatively, these two reservoirs may have formed because of a migrating snowline with no persistent disk gap (*6*). Because the evolution of protoplanetary disks is thought to depend on the coupling of the weakly ionized gas of the disk with large-scale magnetic fields (*7*–*10*), we can search for evidence of disk substructures and explore their origin by studying the paleomagnetism of meteorites that formed in each reservoir.

Previous paleomagnetic measurements of LL chondrites, derived from the noncarbonaceous reservoir, indicate the presence of a disk midplane magnetic field of 54 ± 21 μT at 2.0 ± 0.8 million years (Ma) after the formation of calcium-aluminum–rich inclusion (CAIs) (*11*, *12*). These paleointensities, which were measured from individual chondrules that carry thermoremanent magnetization (TRM) acquired before their accretion onto the LL parent body, provide evidence for the existence of a nebular magnetic field in the noncarbonaceous reservoir. Paleomagnetic studies of CM (*13*), CR (*14*), and CV (*15*) chondrites indicate a field in the carbonaceous reservoir of >6 μT at ~3 Ma after CAI formation, <8 μT at ~3.7 Ma after CAI formation (*10*, *16*), and ≥ 40 μT sometime between ~3-40 Ma after CAI formation (*15*, *17*). However, these records have several key limitations. For instance, the records in CM and CV chondrites are postaccretional chemical remanent magnetizations acquired during parent-body alteration (*13*). This poses two problems: The magnetic record could have been imparted by a parent-body dynamo field rather than from the solar nebula field and the retrieved paleointensity is likely a lower limit (*10*). In addition, the age of the CR record is within error of the estimated lifetime of nebula (*18*), such that it may not constrain the strength of the nebular field during the main period of disk accretion (*10*). Therefore, the intensity of the nebular field in the carbonaceous reservoir is currently poorly constrained.

To obtain robust paleointensity records from the midplane of the solar nebula in the carbonaceous reservoir, we conducted paleomagnetic studies on two CO carbonaceous chondrites: Allan Hills (ALH) A77307 (type 3.03) and Dominion Range (DOM) 08006 (type 3.00) (*19*–*23*). We selected these meteorites because they experienced low peak metamorphic temperatures (200° to 300°C), minor parent-body aqueous alteration, shock pressures below 5 GPa, and minimal terrestrial weathering (weathering grades A/B and Ae, respectively) (*19*–*23*). Therefore, they are unlikely to have been magnetically overprinted following accretion onto the CO parent body, with DOM 08006 in particular being one of the least altered known meteorites (*20*).

Following the previous paleomagnetic study of LL chondrules, we targeted dusty olivine chondrules because they contain high-fidelity paleomagnetic recorders in the form of fine-grained (~25 to 1000 nm) kamacite (α-Fe) crystals formed before accretion onto the parent body (*11*, *24*–*27*). Because chondrules cooled quickly in the protoplanetary disk environment [100° to 1000°C hour^{-1}; (*28*)], they should carry a near-instantaneous TRM record of the nebular field (*11*, *29*, *30*). Al-Mg dating of CO chondrules indicate that this record was acquired 2.2 ± 0.8 Ma after CAI formation (*12*, *31*).

We extracted six 100- to 300-μm-diameter dusty olivine chondrules from both meteorites: two from ALHA77307 (DOC1 and DOC2) and four from DOM 08006 (DOC3, DOC4, DOC5, and DOC6). Three of the DOM 08006 chondrules were split into two subsamples each (DOC3a/DOC3b, DOC5a/DOC5b, and DOC6a/DOC6b) to produce nine total subsamples from both meteorites used for paleomagnetic measurements. All chondrules and chondrule fragments were mutually oriented during extraction and paleomagnetic measurements. Given the chondrules' weak natural remanent magnetization (NRM) (ranging from 1.3×10^{-10} down to 1.7×10^{-12} Am^2 before demagnetization), we obtained magnetic measurements using the superconducting quantum interference device (SQUID) microscope and quantum diamond microscope (QDM) in the Massachusetts Institute of

[1]Department of Earth, Atmospheric and Planetary Sciences, Massachusetts Institute of Technology, Cambridge, MA, USA. [2]Department of Earth Sciences, Oxford University, Oxford, UK. [3]Institute for Advanced Study and Department of Astronomy, Tsinghua University, Beijing, China.
*Corresponding author. Email: caue@mit.edu

Technology (MIT) Paleomagnetism Laboratory (see Materials and Methods) (*32*).

RESULTS

Backscattered electron microscopy (BSE) images and compositional analysis using wavelength dispersive spectrometry (WDS) indicate that the chondrules contain numerous submicrometer diameter inclusions of nearly pure-Fe kamacite (see the Supplementary Materials). Furthermore, QDM imaging confirms that the magnetization-carrying capacity of the chondrules is dominated by these grains rather than by any multidomain metal grains and/or secondary ferromagnetic minerals (see the Supplementary Materials). These fine metal grains are expected to have formed during subsolidus reduction of the chondrules before their accretion on the parent body (*26*). On the basis of their size and composition, many of these grains are predicted to be in the single vortex size range and smaller, which has been shown to have the potential to carry paleomagnetic records over a period longer than the lifetime of the solar system (*11*, *33*).

Our alternating field (AF) demagnetization showed that some subsamples carried a low-coercivity (LC) component blocked up to <20 mT (Fig. 1 and figs. S2 and S3). The LC component may be a viscous remanent magnetization acquired on Earth and/or a weak-field isothermal remanent magnetization acquired during sample handling. After the removal of the LC component, all subsamples were found to contain high-coercivity (HC) components blocked up to at least 50 mT (Fig. 1, figs. S2 and S3, and table S1), with two subsamples having HC components blocked up to 160 and 270 mT (Fig. 1 and fig. S2).

The high AF-stability of the HC components coupled with the pristine conditions of the meteorites suggest that the HC components are likely records of the nebular field. To further test this conclusion, we conducted unidirectionality tests and conglomerate tests (see the Supplementary Materials). Because the nebular field is expected to have been directionally homogeneous on submillimeter length scales, a nebular TRM should be unidirectional within each chondrule. Our measurements confirm this: Pairs of subsamples of three DOM 08006 chondrules have HC directions within each other's maximum angles of deviation (Fig. 2). In addition, if the chondrules have not been remagnetized since parent body accretion (including on their parent body and after arrival on Earth), then they should collectively exhibit random magnetization directions. Our measurements of two chondrules from ALHA77307 and four chondrules from DOM 08006 (Fig. 2) confirm this: We cannot reject the hypothesis that both sets of directions are random with 95% confidence (*34*) (see the Supplementary Materials). In summary, the unidirectionality and conglomerate tests strongly support the conclusion that the chondrules carry robust paleomagnetic records of the solar nebula magnetic field acquired before accretion onto their parent bodies.

To determine the paleointensity of the recorded field, we compared the AF demagnetization of the NRM to that of an anhysteretic remanent magnetization (ARM) acquired in a bias field of 200 μT and a peak AF of up to 145 mT for seven chondrules [following previous studies (*35*)]. Paleointensity estimates were estimated assuming a ratio of ARM to TRM of 1.87 as previously measured for dusty olivine chondrules (see Materials and Methods). The resulting mean HC paleointensity estimates from two ALHA77307 chondrules and

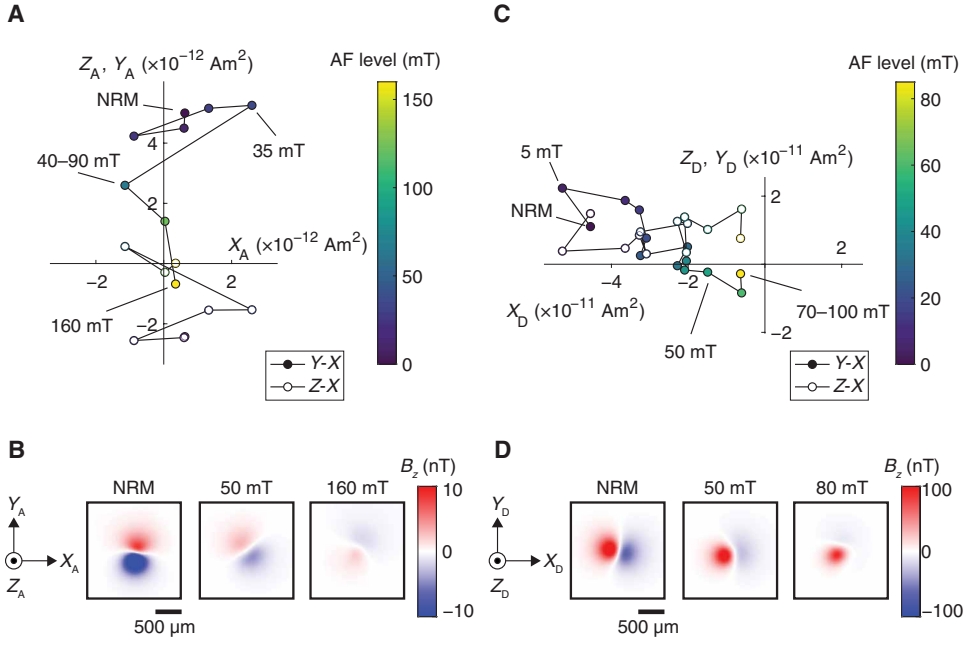

Fig. 1. AF demagnetization of CO dusty olivine chondrules. (**A** and **B**) DOC1 from ALHA77307. (**C** and **D**) DOC4 from DOM 08006. (A and C) Orthographic projections of NRM vector endpoints during alternating field (AF) demagnetization showing averaged measurements for repeated AF steps and across AF levels. Closed symbols show the *Y-X* projection of the magnetic moment, and open symbols show *Z-X* projection of the magnetic moment; subscripts "A" and "D" denote separate coordinate systems for ALHA77307 and DOM 08006, respectively. We interpret the steps between NRM and 160 mT for DOC1 and between 50 and 850 mT for DOC4 as constituting the HC components. Selected demagnetization steps are labeled. Color scales show the AF levels. (B and D) Out-of-the-page magnetic field component (B_z) maps for selected steps measured at a height of ~300 μm above the chondrules obtained with the SQUID microscope. Each map represents one of six maps associated with different applications of the AF field to obtain each step shown in the orthographic projection.

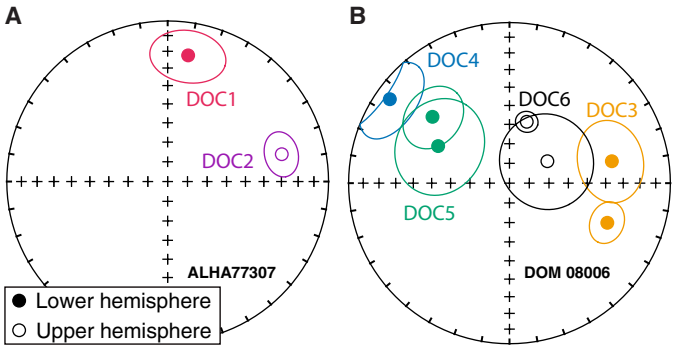

Fig. 2. Direction of the HC components of the dusty olivine chondrules from CO chondrites. (**A**) ALHA77307. (**B**) DOM 08006. Shown are equal area stereographic projections containing directions calculated from principal components analysis and their corresponding maximum angular deviations. Points with different colors are from different individual chondrules, while points with identical colors are subsamples from an individual chondrule. The scattered directions from different chondrules in (A) and (B) indicate that the meteorites were not remagnetized since the chondrules accreted. The clustered directions among subsamples of the same chondrules in (B) are consistent with that expected for a TRM acquired during primary cooling in the solar nebula.

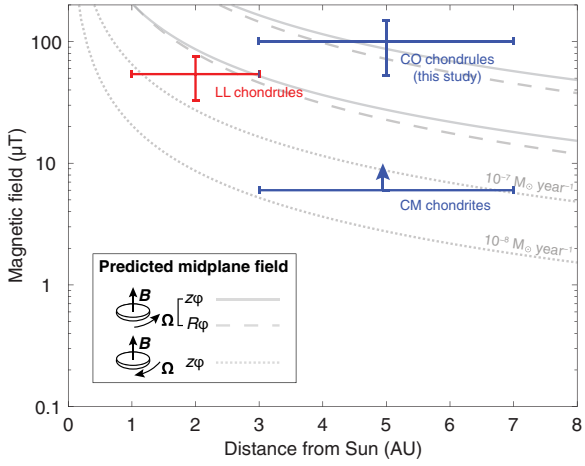

Fig. 3. Comparison between paleomagnetic constraints and model predictions for the solar nebula magnetic field intensity. Shown are paleointensity records from the first 3 Ma after CAI formation: LL chondrules (*11*), CM chondrites (*13*), and CO chondrules (this study). Solid and dashed lines show predicted midplane magnetic field, due to vertical-toroidal [$z\varphi$; equation 3 of (*10*)] and radial-toroidal [$R\varphi$; equation 2 of (*10*)] Maxwell stresses, respectively, assuming the nebular magnetic field and sense of disk rotation are aligned. Dotted lines show the field due to vertical-toroidal Maxwell stresses [$z\varphi$; equation 3 of (*10*)] assuming the nebular magnetic field and sense of disk rotation are antialigned. Top and bottom curves were calculated assuming accretion rates of 10^{-7} and 10^{-8} $M_\odot$ $year^{-1}$, respectively.

five DOM 08006 chondrules are 30 ± 10 μT and 59 ± 31 μT, respectively. Combining the seven samples and accounting for chondrule spinning during TRM acquisition [which decreases the background nebular field intensity recorded by the chondrule by an average factor of 2 (*11*)], we obtained a grand mean paleointensity of the background nebular field of 101 ± 48 μT (table S2).

DISCUSSION

Together with the previous paleomagnetic study of CM chondrites (*13*), the magnetic record from CO chondrules strongly supports the presence of a nebular magnetic field in the carbonaceous reservoir at ~2 to 3 Ma after CAI formation. Furthermore, the data from the CO chondrules provide the first accurate constraints on the intensity of the nebular magnetic field in the carbonaceous reservoir. In particular, the CO chondrule paleointensities are >16 times higher than the lower limit measured from bulk CM chondrites, which highlights the importance of measuring TRMs to obtain robust magnetic records. The identification of magnetic fields in the noncarbonaceous and carbonaceous reservoirs suggests a widespread role for magnetically driven accretion in the early solar system.

The structures and evolution of protoplanetary disks are governed by the mechanisms that drive disk accretion, likely mediated by magnetic fields. The accretion rate scales quadratically with field strength in the disk midplane with a prefactor depending on disk microphysics (especially ionization and field orientation). For a spatially constant accretion rate, the field intensity should decay as $\sim R^{-5/4}$ or $\sim R^{-11/8}$, where R is the radial distance from the Sun, depending on whether accretion is primarily driven by the radial-toroidal ($R\varphi$) or vertical-toroidal ($z\varphi$) components of the Maxwell stress (Fig. 3) (*10*). Because of the Hall effect, the predicted field intensity is a factor of up to ~10 higher if the background field threading the disk is aligned with disk rotation axis compared to the antialigned case. Given typical astronomically observed disk accretion rates of $\sim 1 \times 10^{-8}$ $M_\odot$ $year^{-1}$ (*36*), the measured CO paleointensity strongly favors the scenario of aligned polarity (Fig. 3), which would otherwise lead to an unreasonably large accretion rate ($\sim 1 \times 10^{-5}$ $M_\odot$ $year^{-1}$).

Considering the mean paleointensities from LL and CO chondrules, we find that the accretion rate was highly variable in the early solar system: for a disk with aligned polarity and a net vertical magnetic field ($z\varphi$ only), the accretion rates are $\sim 4^{+4}_{-2} \times 10^{-9}$ $M_\odot$ $year^{-1}$ in the noncarbonaceous reservoir and $\sim 1^{+2}_{-0.6} \times 10^{-7}$ $M_\odot$ $year^{-1}$ in the carbonaceous reservoir (Fig. 3). The observed factor of ~5 to 150 variation in the magnetically driven accretion rate between the two reservoirs could reflect variations in the accretion rate in time and/or in space. Temporal variations would be broadly consistent with astronomically observed accretion bursts in protoplanetary disks that occur on a timescale of hundreds of years (*37*). However, our Monte Carlo simulations suggest that the probability that the observed changes in accretion are due to temporal fluctuations is <0.4% (see the Supplementary Materials). Thus, our results favor the presence of a spatial mismatch in the magnetically driven accretion rates between the two reservoirs. This spatial mismatch in the accretion rate has also been observed in recent paleomagnetic measurements of the CV chondrite Allende (*15*). While a spatial variation in accretion rate has also been proposed to explain the anomalously weak fields recorded by CR chondrules, it was not possible to conclusively differentiate between varying accretion rates or a null magnetic record because of the prior dissipation of the solar nebula in those samples (*10*).

The observed mismatch in the accretion rates requires a mechanism that removed mass from the accretion flux between the carbonaceous and the noncarbonaceous reservoirs. If proto-Jupiter or another giant planet was present between the two reservoirs, then it is possible that part of this accretion flux was intercepted and accreted onto the growing planet. However, if the mismatch was completely

due to accretion onto proto-Jupiter, that would require a growth time scale of just ~10,000 years for the planet. This is several orders of magnitude faster than the several–million year time scale predicted by the core accretion model, the favored mechanism for Jupiter formation (*38*). Alternatively, a large fraction of accretion mass flux could be lost through a disk outflow. A substantial mass loss has been predicted in theoretical models of photoevaporation leading to inside-out disk clearing [e.g., (*39*–*41*)]. On the other hand, given the likely role magnetic fields in driving disk accretion, photoevaporation and magnetized disk winds may operate concurrently (*42*, *43*), leading to magnetothermal disk winds whose mass loss rates are comparable to or exceed that of observed accretion rates of protoplanetary disks. This is sufficient to account for our observed mismatch in accretion rates and potentially lead to the formation of an inner cavity (i.e., extreme version of a gap) (*44*). Note, however, that this scenario does not preclude a role for Jupiter in gap formation. Its presence would likely accelerate the formation of the cavity (*45*), transforming the solar nebula into a transition disk.

In summary, we present a robust record of magnetic fields in the carbonaceous reservoir of the solar nebula. When compared to previous measurements of magnetic fields from the noncarbonaceous reservoir and models that describe the magnetic field in protoplanetary disks, we observe that the accretion rate in the carbonaceous reservoir is several times higher than that of the noncarbonaceous reservoir, implying the presence of a mismatch in accretion rates. This mismatch may be associated with disk mass loss through the presence of a gas giant, photoevaporation, and/or magnetized winds. These mechanisms could produce a disk substructure like those observed astronomically and like that inferred from the isotopic dichotomy measured among various meteorites in the early solar system.

MATERIALS AND METHODS

Chondrule extraction and orientation

Bulk samples of ALHA77307,157 (0.57 g) and DOM 08006,102 (2.8 g) were obtained from the NASA Johnson Space Center. At MIT, oriented thick sections were cut from these using a wire saw cooled with ethanol during cutting. Each thick section had an average area of 4 cm^2 and a thickness of ~500 μm. The thick sections were then polished down to 1-μm roughness, and dusty olivine chondrules were identified using reflected light microscopy. Overall, we found that dusty olivine chondrules are very rare among CO chondrites, with a frequency of only ~1 out of 100 chondrules (~0.005 inclusion mm^{-3}). The six dusty olivine chondrules used in this study were obtained from two thick sections from ALHA77307 and eight from DOM 08006. We note that some thick sections did not contain identifiable dusty olivine chondrules. All extracted chondrules were at least 3 mm away from the fusion crust of the parent sample (table S1).

Figure S1 shows the procedure for chondrule extraction. Before extraction, the thick section surface orientation was documented using imaging with a petrographic microscope (step 1, fig. S1). A region of ~300 to 500 μm in thickness was excavated around the target chondrule using a degaussed carbide dental drill bit (step 2, fig. S1). After excavation, we used two different techniques to extract the chondrules. In the first technique, chondrule samples DOC1, DOC2, DOC3a, and DOC3b were extracted using a degaussed dental drill bit (step 3, fig. S1), and a pipette with isopropyl alcohol was used to transfer the sample to a nonmagnetic quartz disk. The samples were then glued to the quartz disk using cyanoacrylate cement. While the glue hardened, we oriented the sample by comparing its surface with the previously acquired image of the chondrule in situ. In the second technique, chondrule samples DOC4, DOC5a, DOC5b, DOC6a, and DOC6b each had a ~400 μm by 400 μm by 1000 μm nonmagnetic quartz glass coverslip glued with cyanoacrylate cement onto their top surfaces (step 3, fig. S1). We then marked the glass with a marker to orient it with respect to the thick section. The chondrules were then extracted using a degaussed dental drill bit and mounted on a quartz glass with cyanoacrylate cement. After extraction, we added Kapton tape as standoffs that were at least 2 mm away from the samples (step 4, fig. S1). The standoffs were added such that they were slightly higher than the samples, protecting the samples from rubbing against the SQUID microscope window during the magnetic measurements. Table S1 shows the orientations of the chondrules during the SQUID microscope measurements. We estimate that the extraction and mounting techniques can add up to 15° of total angular uncertainty.

Paleomagnetism

We used AFs to demagnetize the chondrules in steps of 5 or 10 mT, using an automatic 3-axis degausser system integrated into the 2G Enterprises Superconducting Rock Magnetometer 755R (*46*) at MIT. We demagnetized the samples with repeated AF applications to reduce spurious ARM and used the Zijderveld-Dunlop averaging method to correct for gyroremanent magnetization (*47*). The maximum AF field necessary to demagnetize the samples varied among our samples. Sample DOC1 was demagnetized up to 400 mT, DOC2 up to 410 mT, DOC3a up to 100 mT, DOC3b up to 60 mT, DOC4 up to 100 mT, DOC5a up to 60 mT, DOC5b up to 75 mT, DOC6a up to 70 mT, and DOC6b up to 100 mT. For each AF step, we measured the magnetic field of each sample six times: once after applications of the AF in the *X*, *Y*, and *Z* directions successively, twice after applications in the *X* direction, twice after applications in the *Y* direction, and once after an application in the *Z* direction.

NRM measurements were obtained using the SQUID microscope in the MIT Paleomagnetism Laboratory (*32*). Measurements of the samples' magnetic fields were obtained at an effective sensor-to-sample distance of ~300 μm (*32*). For samples found to be dipolar magnetic field sources (DOC1, DOC2, DOC3a, DOC3b, DOC4, DOC5b, and DOC6b), we used a previously described inversion technique to obtain the magnetic moment from the magnetic field (*48*). For samples DOC5a and DOC6a, whose fields were found to be nondipolar, we upward-continued the magnetic maps by 150 μm and retrieved their dipole moments using averages from a first- to the fifth- and second-degree multipole model, respectively. After obtaining magnetic moments from each AF step, we averaged across the six steps and sometimes also across AF levels. The directions of NRM components were calculated using principal components analysis (*49*). The demagnetization projections are shown in figs. S2 and S3. If a NRM component had a deviation angle less than the maximum angle deviation, then this component was inferred to be the characteristic component and therefore anchored to the origin (*49*, *50*). Table S1 shows the results of the principal components analysis including the levels that were averaged.

To obtain paleointensities, we used the ARM method (*11*, *35*) for which

$$B_{\text{paleo}} = \frac{B_{\text{lab}}}{f'} \frac{\Delta \text{NRM}}{\Delta \text{ARM}} \quad (1)$$

where B_{paleo} is the ancient magnetic field recovered from the experiment, B_{lab} is the 200-μT ARM bias magnetic field applied to the sample, ΔNRM and ΔARM are the respective changes in magnetic moment during the demagnetization of the NRM and the ARM, and *f'* is the ratio of TRM to ARM. The ARM was applied with a peak AF field of 145 mT for DOC1 and DOC2, 100 mT for DOC3a, 60 mT for DOC3b, 100 mT for DOC4, 75 mT for DOC5b, and 100 mT for DOC6b. We AF demagnetized the ARM using the same sequence used for the NRM. All samples used for paleointensity determination were nearly dipolar sources, such that we used the inversion technique for dipolar sources described above. Following previous paleomagnetic studies of dusty olivine chondrules, we adopted an experimentally determined value for *f'* of 1.87 (*11*, *27*).

Figures S5 and S6 show the results of the paleointensity experiments. For all samples except DOC3a, we fit for ΔNRM/ΔARM using reduced major axis least squares. For DOC3a, we used ordinary least squares because the correlation parameter was <0.6 (*51*). ΔNRM was calculated by vector subtraction from the first demagnetization step in the HC component fit, while ΔARM was calculated by subtraction from the first acquired ARM step. Table S5 shows a summary of the paleointensities and their quality criteria.

Mineralogy

Mineral compositions (fig. S4 and tables S3 and S4) were analyzed on a JEOL JXA-8200 Superprobe electron probe microanalyzer (EPMA) using WDS in the MIT Electron Microprobe Facility. BSE images were obtained with the same instrument (fig. S4). The EPMA was operated at an accelerating voltage of 15 kV and a beam current of 10 nA, and natural and synthetic standards were used for calibration. The counting times were typically 40 s per element, and the 1σ SDs of the accumulated counts were 0.5 to 1.0% from counting statistics. The raw data were corrected for matrix effects using the CITZAF package (*52*). To identify the origin of the magnetic signal of these two samples, we mapped the magnetization of chondrules using the QDM at MIT (fig. S4) (*53*, *54*). The sensor to sample distance was ~5 μm, and the map resolution was 1.17 μm. The QDM maps were obtained after the demagnetization of an ARM applied to DOC2 (200 μT bias with an AF of 145 mT) to 145 mT (fig. S4C) and after the application of an ARM (200 μT bias with an AF of 100 mT) to DOC6b (fig. S4F).

SUPPLEMENTARY MATERIALS

Supplementary material for this article is available at https://science.org/doi/10.1126/sciadv.abj6928

REFERENCES AND NOTES

1. S. M. Andrews, Observations of protoplanetary disk structures. *Annu. Rev. Astron. Astrophys.* **58**, 483–528 (2020).
2. T. S. Kruijer, T. Kleine, L. E. Borg, The great isotopic dichotomy of the early solar system. *Nat. Astron.* **4**, 32–40 (2020).
3. E. R. D. Scott, A. N. Krot, I. S. Sanders, Isotopic dichotomy among meteorites and its bearing on the protoplanetary disk. *Astrophys. J.* **854**, 164 (2018).
4. T. Kleine, G. Budde, C. Burkhardt, T. S. Kruijer, E. A. Worsham, A. Morbidelli, F. Nimmo, The non-carbonaceous–carbonaceous meteorite dichotomy. *Space Sci. Rev.* **216**, 55 (2020).
5. R. Brasser, S. J. Mojzsis, The partitioning of the inner and outer solar system by a structured protoplanetary disk. *Nat. Astron.* **4**, 492–499 (2020).
6. T. Lichtenberg, J. Drążkowska, M. Schönbächler, G. J. Golabek, T. O. Hands, Bifurcation of planetary building blocks during Solar System formation. *Science* **371**, 365–370 (2021).
7. X.-N. Bai, J. Goodman, Heat and dust in active layers of protostellar disks. *Astrophys. J.* **701**, 737–755 (2009).
8. X.-N. Bai, Global simulations of the inner regions of protoplanetary disks with comprehensive disk microphysics. *Astrophys. J.* **845**, 75 (2017).
9. N. J. Turner, S. Fromang, C. Gammie, H. Klahr, G. Lesur, M. Wardle, X.-N. Bai, in *Protostars and Planets VI*, H. Beuther, R. S. Klessen, C. P. Dullemond, T. K. Henning, Eds. (University of Arizona Press, 2014), pp. 411–432.
10. B. P. Weiss, X.-N. Bai, R. R. Fu, History of the solar nebula from meteorite paleomagnetism. *Sci. Adv.* **7**, eaba5967 (2021).
11. R. R. Fu, B. P. Weiss, E. A. Lima, R. J. Harrison, X. N. Bai, S. J. Desch, D. S. Ebel, C. Suavet, H. Wang, D. Glenn, D. le Sage, T. Kasama, R. L. Walsworth, A. T. Kuan, Solar nebula magnetic fields recorded in the Semarkona meteorite. *Science* **346**, 1089–1092 (2014).
12. N. T. Kita, T. Ushikubo, Evolution of protoplanetary disk inferred from ^{26}Al chronology of individual chondrules. *Meteorit. Planet. Sci.* **47**, 1108–1119 (2011).
13. C. Cournède, J. Gattacceca, M. Gounelle, P. Rochette, B. P. Weiss, B. Zanda, An early solar system magnetic field recorded in CM chondrites. *Earth Planet. Sci. Lett.* **410**, 62–74 (2015).
14. R. R. Fu, P. Kehayias, B. P. Weiss, D. L. Schrader, X.-N. Bai, J. B. Simon, Weak magnetic fields in the outer solar nebula recorded in CR chondrites. *J. Geophys. Res.* **125**, e2019JE006260 (2020).
15. R. R. Fu, M. W. R. Volk, D. Bilardello, D. Libourel, G. R. J. Lesur, O. Ben Dor, The fine-scale magnetic history of the Allende meteorite: implications for the structure of the solar nebula. *AGU Adv.* **2**, e2021AV000486 (2021).
16. D. L. Schrader, K. Nagashima, A. N. Krot, R. C. Ogliore, Q. Z. Yin, Y. Amelin, C. H. Stirling, A. Kaltenbach, Distribution of ^{26}Al in the CR chondrite chondrule-forming region of the protoplanetary disk. *Geochim. Cosmochim. Acta* **201**, 275–302 (2017).
17. L. Carporzen, B. P. Weiss, L. T. Elkins-Tanton, D. L. Shuster, D. S. Ebel, J. Gattacceca, Magnetic evidence for a partially differentiated carbonaceous chondrite parent body. *Proc. Natl. Acad. Sci. U.S.A.* **108**, 6386–6389 (2011).
18. H. Wang, B. P. Weiss, X.-N. Bai, B. G. Downey, J. Wang, J. Wang, C. Suavet, R. R. Fu, M. E. Zucolotto, Lifetime of the solar nebula constrained by meteorite paleomagnetism. *Science* **355**, 623–627 (2017).
19. L. Bonal, M. Bourot-Denise, E. Quirico, G. Montagnac, E. Lewin, Organic matter and metamorphic history of CO chondrites. *Geochim. Cosmochim. Acta* **71**, 1605–1623 (2007).
20. J. Davidson, C. M. O.'D. Alexander, R. M. Stroud, H. Busemann, L. R. Nittler, Mineralogy and petrology of Dominion Range 08006: A very primitive CO3 carbonaceous chondrite. *Geochim. Cosmochim. Acta* **265**, 259–278 (2019).
21. C. M. O.'D. Alexander, R. C. Greenwood, R. Bowden, J. M. Gibson, K. T. Howard, I. A. Franchi, A mutli-technique search for the most primitive CO chondrites. *Geochim. Cosmochim. Acta* **221**, 406–420 (2018).
22. E. R. D. Scott, K. Keil, D. Stöffler, Shock metamorphism of carbonaceous chondrites. *Geochim. Cosmochim. Acta* **56**, 4281–4293 (1992).
23. C. M. O.'D. Alexander, M. Fogel, H. Yabuta, G. D. Cody, The origin and evolution of chondrites recorded in the elemental and isotopic compositions of their macromolecular organic matter. *Geochim. Cosmochim. Acta* **71**, 4380–4403 (2007).
24. J. Shah, W. Williams, T. P. Almeida, L. Nagy, A. R. Muxworthy, A. Kovács, M. A. Valdez-Grijalva, K. Fabian, S. S. Russell, M. J. Genge, The oldest magnetic record in our solar system identified using nanometric imaging and numerical modeling. *Nat. Commun.* **9**, 1–6 (2018).
25. J. F. Einsle, R. J. Harrison, T. Kasama, P. Ó. Conbhuí, K. Fabian, W. Williams, L. Woodland, R. R. Fu, B. P. Weiss, P. A. Midgley, Multi-scale three-dimensional characterization of iron particles in dusty olivine: Implications for paleomagnetism of chondritic meteorites. *Am. Mineral.* **101**, 2070–2084 (2016).
26. S.-C. L. L. Lappe, N. S. Church, T. Kasama, A. B. da Silva Fanta, G. Bromiley, R. E. Dunin-Borkowski, J. M. Feinberg, S. Russell, R. J. Harrison, Mineral magnetism of dusty olivine: A credible recorder of pre-accretionary remanence. *Geochem. Geophys. Geosyst.* **12**, Q12Z35 (2011).
27. S.-C. L. L. Lappe, J. M. Feinberg, A. Muxworthy, R. J. Harrison, Comparison and calibration of nonheating paleointensity methods : A case study using dusty olivine. *Geochem. Geophys. Geosyst.* **14**, 2143–2158 (2013).
28. E. R. D. Scott, A. N. Krot, in *Treatise on Geochemistry, vol. 2 of Planets, Asteroids, Comets, and the Solar System*, H. D. Holland, K. K. Turekian, Eds. (Elsevier Science, 2013), pp. 66–137.
29. S. J. Desch, M. A. Morris, H. C. Connolly Jr., A. P. Boss, The importance of experiments: Constraints on chondrule formation models. *Meteorit. Planet. Sci.* **47**, 1139–1156 (2012).
30. S. J. Desch, M. A. Morris, H. C. Connolly Jr., A. P. Boss, A critical examination of the X-wind model for chondrule and calcium-rich, aluminum-rich inclusion formation and radionuclide production. *Astrophys. J.* **725**, 692–711 (2010).
31. Recent high-precision Al-Mg ages of LL chondrules support a shorter formation interval than previous Al-Mg ages. See Supplementary Text for more information.
32. B. P. Weiss, E. A. Lima, L. E. Fong, F. J. Baudenbacher, Paleomagnetic analysis using SQUID microscopy. *J. Geophys. Res.* **112**, B09105 (2007).

33. L. Nagy, W. Williams, L. Tauxe, A. R. Muxworthy, I. Ferreira, Thermomagnetic recording fidelity of nanometer-sized iron and implications for planetary magnetism. *Proc. Natl. Acad. Sci. U.S.A.* **116**, 1984–1991 (2019).
34. G. S. Watson, A test for randomness of directions. *Geophys. J. Int.* **7**, 160–161 (1956).
35. S. M. Tikoo, B. P. Weiss, W. S. Cassata, D. L. Shuster, J. Gattacceca, E. A. Lima, C. Suavet, F. Nimmo, M. D. Fuller, Decline of the lunar core dynamo. *Earth Planet. Sci. Lett.* **404**, 89–97 (2014).
36. L. Hartmann, N. Calvet, E. Gullbring, P. D'Alessio, Accretion and the evolution of T Tauri disks. *Astrophys. J.* **495**, 385–400 (1998).
37. L. Hartmann, G. Herczeg, N. Calvet, Accretion onto pre-main-sequence stars. *Annu. Rev. Astron. Astrophys.* **54**, 135–180 (2016).
38. S. K. Atreya, A. Crida, T. Guillot, J. I. Lunine, N. Madhusudhan, O. Mousis, in *Saturn in the 21st Century*, K. H. Baines, F. M. Flasar, N. Krupp, T. Stallard, Eds. (Cambridge Univ. Press, 2018), pp. 5–43.
39. C. J. Clarke, A. Gendrin, M. Sotomayor, The dispersal of circumstellar discs: The role of the ultraviolet switch. *Mon. Not. R. Astron. Soc.* **328**, 485–491 (2001).
40. J. E. Owen, C. J. Clarke, B. Ercolano, On the theory of disc photoevaporation. *Mon. Not. R. Astron. Soc.* **422**, 1880–1901 (2012).
41. G. Picogna, B. Ercolano, J. E. Owen, M. L. Weber, The dispersal of protoplanetary discs – I. A new generation of X-ray photoevaporation models. *Mon. Not. R. Astron. Soc.* **487**, 691–701 (2019).
42. L. Wang, X.-N. Bai, J. Goodman, Global simulations of protoplanetary disk outflows with coupled non-ideal magnetohydrodynamics and consistent thermochemistry. *Astrophys. J.* **874**, 90 (2019).
43. X.-N. Bai, Toward a global evolutionary model of protoplanetary disks. *Astrophys. J.* **821**, 80 (2016).
44. T. K. Suzuki, M. Ogihara, A. Morbidelli, A. Crida, T. Guillot, Evolution of protoplanetary discs with magnetically driven disc winds. *Astron. Astrophys.* **596**, A74 (2016).
45. G. P. Rosotti, B. Ercolano, J. E. Owen, P. J. Armitage, The interplay between x-ray photoevaporation and planet formation. *Mon. Not. R. Astron. Soc.* **430**, 1392–1401 (2013).
46. J. L. Kirschvink, R. E. Kopp, T. D. Raub, C. T. Baumgartner, J. W. Holt, Rapid, precise, and high-sensitivity acquisition of paleomagnetic and rock-magnetic data: Development of a low-noise automatic sample changing system for superconducting rock magnetometers. *Geochem. Geophys. Geosyst.* **9**, Q05Y01 (2008).
47. A. Stephenson, Three-axis static field demagnetization of rocks and the identification of natural remanent magnetization, gyroremanent magnetization, and anisotropy. *J. Geoph. Res.* **98**, 373–381 (1993).
48. E. A. Lima, B. P. Weiss, Ultra-high sensitivity moment magnetometry of geological samples using magnetic microscopy. *Geochem. Geophys. Geosyst.* **17**, 3754–3774 (2016).
49. J. L. Kirschvink, The least-squares line and plane and the analysis of palaeomagnetic data. *Geophys. J. R. Astr. Soc.* **62**, 699–718 (1980).
50. L. Tauxe, H. Staudigel, Strength of the geomagnetic field in the Cretaceous Normal Superchron: New data from submarine basaltic glass of the Troodos Ophiolite. *Geochem. Geophys. Geosyst.* **5**, Q02H06 (2004).
51. R. J. Smith, Use and misuse of the reduced major axis for line-fitting. *Am. J. Phys. Anthropol.* **140**, 476–486 (2009).
52. J. T. Armstrong, CITZAF: A package of correction programs for the quantitative electron microbeam X-ray analysis of thick polished materials, thin films, and particles. *Microbeam Anal.* **4**, 177–200 (1995).
53. R. R. Fu, E. A. Lima, M. W. R. Volk, R. Trubko, High sensitivity moment magnetometry with the quantum diamond microscope. *Geochem. Geophys. Geosyst.* **21**, e2020GC009147 (2020).
54. D. R. Glenn, R. R. Fu, P. Kehayias, D. Le Sage, E. A. Lima, B. P. Weiss, R. L. Walsworth, Micrometer-scale magnetic imaging of geological samples using a quantum diamond microscope. *Geochem. Geophys. Geosyst.* **18**, 3254–3267 (2017).
55. S. Ebert, J. Render, G. A. Brennecka, C. Burkhardt, A. Bischoff, S. Gerber, T. Kleine, Ti isotopic evidence for a non-CAI refractory component in the inner solar system. *Earth Planet. Sci. Lett.* **498**, 257–265 (2018).
56. J. M. Schneider, C. Burkhardt, Y. Marrocchi, G. A. Brennecka, T. Kleine, Early evolution of the solar accretion disk inferred from Cr-Ti-O isotopes in individual chondrules. *Earth Planet. Sci. Lett.* **551**, 116585 (2020).
57. F. E. DeMeo, B. Carry, Solar system evolution from compositional mapping of the asteroid belt. *Nature* **505**, 629–634 (2014).
58. A. Morbidelli, K. J. Walsh, D. P. O'Brien, D. A. Minton, W. F. Bottke, in *Asteroids IV*, P. Michel, F. E. DeMeo, W. F. Bottke, Eds. (University of Arizona, 2015), pp. 493–507.
59. S. Sutton, C. M. O.'D. Alexander, A. Bryant, A. Lanzirotti, M. Newville, E. A. Cloutis, The bulk valence state of Fe and the origin of water in chondrites. *Geochim. Cosmochim. Acta* **211**, 115–132 (2017).
60. L. Testi, T. Birnstiel, L. Ricci, S. Andrews, J. Blum, J. Carpenter, C. Dominik, A. Isella, A. Natta, J. P. Williams, D. J. Wilner, in *Protostars and Planets VI*, H. Beuther, R. S. Klessen, C. P. Dullemond, T. K. Henning, Eds. (University of Arizona Press, 2014), pp. 339–361.
61. S. J. Desch, A. Kalyaan, C. M. O.'D. Alexander, The effect of Jupiter's formation on the distribution of refractory elements and inclusions in meteorites. *Astrophys. J. Suppl. S.* **238**, 11 (2018).
62. P. A. Selkin, J. S. Gee, L. Tauxe, W. P. Meurer, A. J. Newell, The effect of remanence anisotropy on paleointensity estimates: A case study from the Archean Stillwater Complex. *Earth Planet. Sci. Lett.* **183**, 403–416 (2000).
63. G. Siron, K. Fukuda, M. Kimura, N. T. Kita, New constraints from ^{26}Al-^{26}Mg chronology of anorthite bearing chondrules in unequilibrated ordinary chondrites. *Geochim. Cosmochim. Acta* **293**, 103–126 (2021).
64. G. Siron, N. T. Kita, K. Fukuda, M. Kimura, in *Lunar and Planetary Science Conference* (2021), p. 1639.
65. A. T. Hertwig, M. Kimura, T. Ushikubo, C. Defouilloy, N. T. Kita, The ^{26}Al-^{26}Mg systematics of FeO-rich chondrules from Acfer 094: Two chondrule generations distinct in age and oxygen isotope ratios. *Geochim. Cosmochim. Acta* **253**, 111–126 (2019).
66. K. Nagashima, A. N. Krot, M. Komatsu, ^{26}Al–^{26}Mg systematics in chondrules from Kaba and Yamato 980145 CV3 carbonaceous chondrites. *Geochim. Cosmochim. Acta* **201**, 303–319 (2017).

Acknowledgments: We thank K. Righter and the Meteorite Working Group for allocating the samples, R. Fu and N. Kita for helpful discussions, and R. Walsworth and R. Fu for sharing quantum diamond microscopy technology and techniques. **Funding:** This study was supported by NASA Discovery program (grant NNM16AA09C) and by the NSF (grant DMS-1521765). **Author contributions:** Conceptualization: C.S.B. and B.P.W. Methodology: C.S.B., B.P.W., and E.A.L. Investigation: C.S.B. and B.P.W. Interpretation: C.S.B., B.P.W., J.F.J.B., and X.-N.B. Visualization: C.S.B. Supervision: B.P.W. Writing—initial drafts: C.S.B. and B.P.W. Writing—review and editing: B.P.W., J.F.J.B., X.-N.B., E.A.L., N.C., and E.N.M. Funding acquisition: B.P.W. **Competing interests:** The authors declare that they have no competing interests; **Data and materials availability:** All data needed to evaluate the conclusions in the paper are present in the paper and available through the Magnetics Information Consortium (MagIC) Database (doi: 10.7288/V4/MAGIC/17129).

Submitted 26 May 2021
Accepted 25 August 2021
Published 15 October 2021
10.1126/sciadv.abj6928

Citation: C. S. Borlina, B. P. Weiss, J. F. J. Bryson, X.-N. Bai, E. A. Lima, N. Chatterjee, E. N. Mansbach, Paleomagnetic evidence for a disk substructure in the early solar system. *Sci. Adv.* **7**, eabj6928 (2021).

ScienceAdvances

Paleomagnetic evidence for a disk substructure in the early solar system

Cauê S. BorlinaBenjamin P. WeissJames F. J. BrysonXue-Ning BaiEduardo A. LimaNilanjan ChatterjeeElias N. Mansbach

Sci. Adv., 7 (42), eabj6928.

Science Advances (ISSN) is published by the American Association for the Advancement of Science. 1200 New York Avenue NW, Washington, DC 20005. The title *Science Advances* is a registered trademark of AAAS.

Science Advances
AAAS

Supplementary Materials for

Paleomagnetic evidence for a disk substructure in the early solar system

Cauê S. Borlina*, Benjamin P. Weiss, James F. J. Bryson, Xue-Ning Bai, Eduardo A. Lima, Nilanjan Chatterjee, Elias N. Mansbach

*Corresponding author. Email: caue@mit.edu

Published 15 October 2021, *Sci. Adv.* **7**, eabj6928 (2021)
DOI: 10.1126/sciadv.abj6928

This PDF file includes:

Supplementary Text

1. Formation Region of Chondrules from the Carbonaceous Chondrites

The existence of a dichotomy in various isotopic systems (e.g., Ti, Mo, Cr, O, Ru, W, Ni) for bulk meteorite samples provides evidence that carbonaceous and non-carbonaceous meteorites may have formed in two distinct reservoirs (*2*, *3*). An equivalent dichotomy is also observed between chondrules from ordinary chondrites [i.e., LL chondrules (*11*)] and carbonaceous chondrites [i.e., CO chondrules (*3*, *55*, *56*)]. The exact location and nature of these reservoirs is still under debate. Nonetheless, because carbonaceous chondrites are likely derived from the water rich C-type asteroids (*57*, *58*), we take their current location at >3 AU as a reference for the location of the carbonaceous reservoir in the early solar system. Furthermore, measurements of the isotopic composition of water in carbonaceous meteorites suggests that most of these samples did not originate beyond 7 AU (*59*). Finally, astronomical observations indicate that meteorites and their components likely formed in the midplane region of the protoplanetary disk (*10*, *60*). Thus, we take the formation region of the CO chondrules to be somewhere between 3-7 AU in the midplane of the early solar system. These regions are similar to, although more restrictive than, the formation regions envisaged by ref. (*6*) and less restrictive than estimated by ref. (*61*).

2. Paleomagnetic Tests to Determine the Origin of the Magnetization

Two paleomagnetic tests were conducted to determine the robustness and the origin of the high coercivity (HC) magnetization of the chondrules: the unidirectionality test and the conglomerate test (*11*). For a magnetization acquired by a chondrule in a uniform background field, we expect subsamples of the same chondrule to have HC paleodirections within error of one another. To test this, we split three chondrules (DOC3, DOC5, and DOC6) into two mutually oriented pieces, each of which we then AF demagnetized and measured (Fig. 2). Comparing the HC directions for the subsamples from each chondrule, we found that all three pairs of subsamples have internally consistent HC magnetization orientations, with mean directions within each other's MADs, supporting our conclusion that the dusty olivine chondrules acquired a stable, homogeneous TRM.

The conglomerate test establishes whether chondrules have been remagnetized since their accretion onto the CO parent body. Remagnetization can occur due to post-accretional thermal metamorphism and/or aqueous alteration on the parent body, heating during atmospheric entry, secondary magnetic minerals produced during terrestrial weathering, and/or and isothermal remanent magnetization (IRM) during sample handling. Because the chondrules were accreted onto the parent body in random directions, chondrules that have not been remagnetized since accretion should exhibit random HC directions. This is indeed what we observe (Fig. 2). Using Eqs. (3) and (4) from ref. (*34*), we calculated the critical value R_0 that the resultant of N nonrandomly oriented unit vectors exceeds 95% of the time. We then we compared this with the length of the resultant of the HC vectors for chondrules from each meteorite, R. When $R < R_0$, we cannot reject the hypothesis that the vectors are random with 95% confidence. Table S2 summarizes the results for the chondrules from ALHA 77307 and DOM 08006, showing that the random hypothesis cannot be rejected with 95% confidence for both samples. This shows that chondrules from both samples were not remagnetized since their accretion to the parent body.

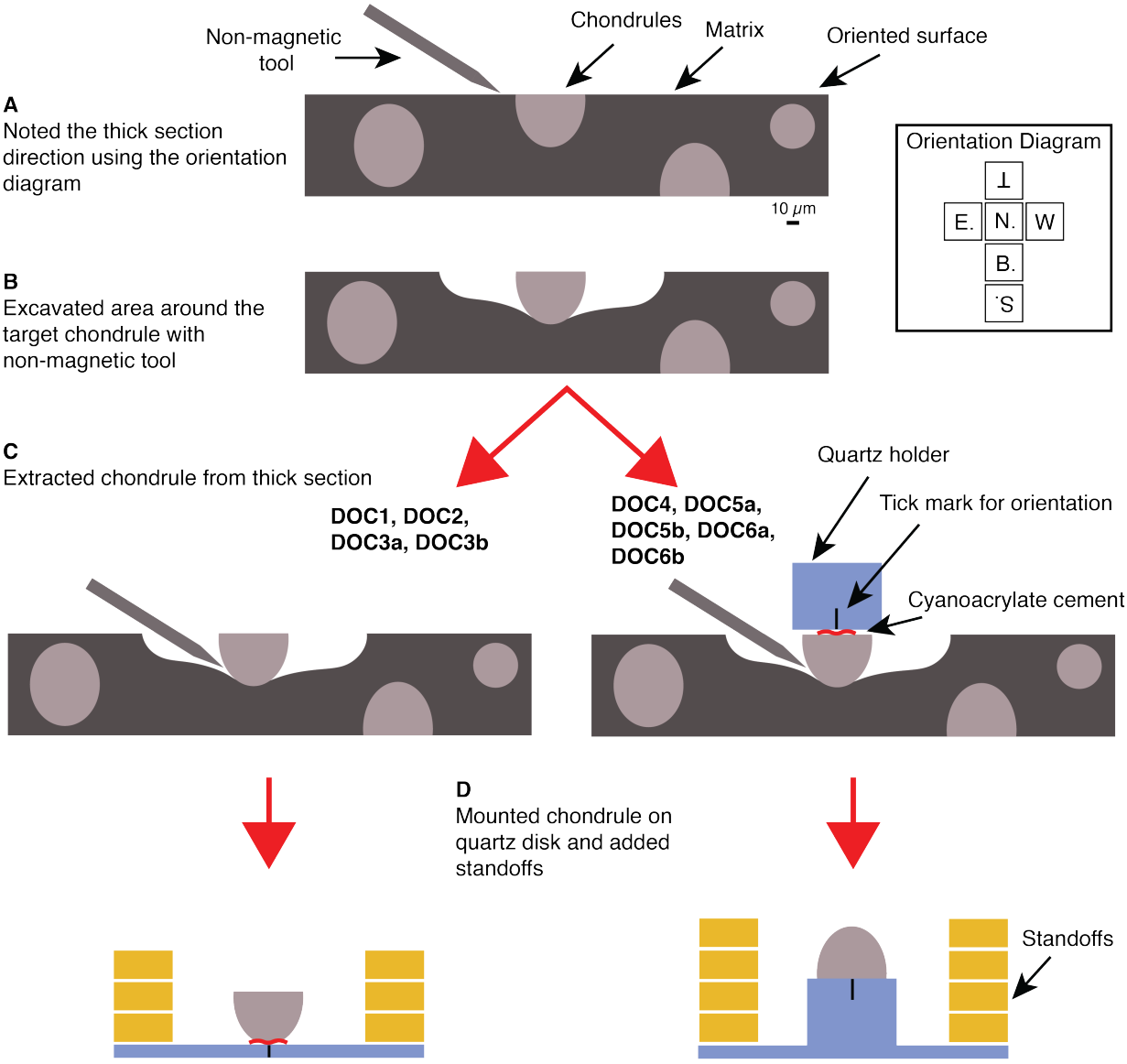

Fig. S1. Schematic showing the sample mounting procedure. (A) Oriented thick sections from the meteorites ALHA 77307 and DOM 08006 were cut and then polished. Dusty olivine targets were identified using reflective light. Orientation diagram is shown on the top right. **(B)** A region around the sample was excavated prior to chondrule extraction. **(C)** Chondrules were extracted using two methods described in the text. **(D)** Samples were mounted on nonmagnetic quartz disks with standoffs to protect sample from rubbing against the SQUID microscope window.

3. Mineralogy of the chondrules

Fig. S4 shows the BSE images (Figs. S4A and D) together with interpretations of the WDS data (Figs. S4B and E) for each sample. Tables S3-S4 summarize the measurements from the WDS analyses for distinct grains. In both samples, we observe the presence of micrometer and sub-micrometer sized Fe kamacite (α-Fe) inclusions in forsterite (Tables S3 and S4) supporting the identification of these inclusions as dusty olivine chondrules (*25*). In DOC2, only we also observed

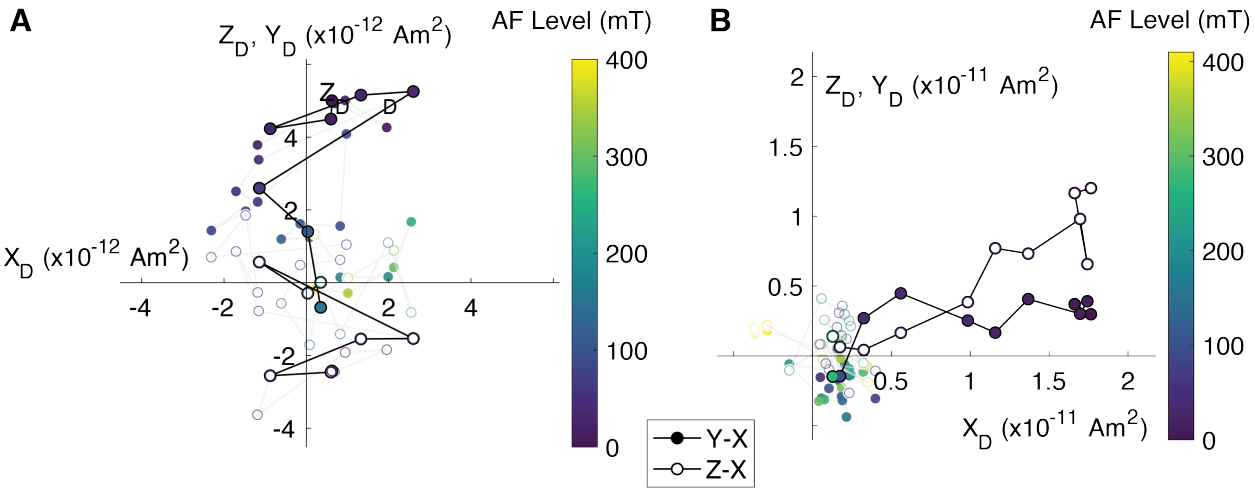

Fig. S2. AF demagnetization of dusty olivine chondrules from ALHA 77307. (**A**) DOC1. (**B**) DOC2. Shown are orthographic projections of the NRM vector endpoints. Closed symbols show the Y-X projection of the moment; open symbols show Z-X projection of the moment. Samples were oriented in the same coordinate system as samples shown in Fig. 1A-B. Colorbar shows the AF level of the steps. Opaque symbols denote datapoints averaged across multiple AF levels while semi-transparent symbols denote unaveraged data. Averaged levels are summarized in the Table S1.

a single martensite (α_2-$Fe_{68}Ni_{20}$) and single magnetite inclusion, with the latter likely associated with minor alteration on the parent-body.

Figs. S4C and S4F show quantum diamond microscopy (QDM) maps showing demagnetized NRM (Fig. S4C) and an ARM acquisition (Fig. S4F) of the same samples that we obtained BSE images and conducted WDS analysis. We observe from both maps that the distribution of the magnetic field is uniform, consistent with the presence of fine Fe grains distributed uniformly throughout the sample's volumes. This spatial distribution is characteristic of the iron metal in dusty olivine chondrules. These maps are also inconsistent with large concentrations of Fe on the grain exterior and/or along cracks where secondary minerals typically form during aqueous alteration. Overall, these observations further support our conclusion that these chondrules contain a magnetic record of the nebular field formed prior to their accretion on the parent body.

4. Assessing Remanence Anisotropy

Anisotropy in samples can bias paleointensity and paleodirection estimates (*62*). To establish if our chondrules required anisotropy corrections, we conducted consecutive ARM acquisitions for each chondrule. Fig. S7 shows ARM acquisitions in a 200 μT bias field for the samples from which we obtained paleointensities. We used an AC field of 400 mT for DOC1, 410 mT for DOC2, 100 mT for DOC3a, 60 mT for DOC3b, 100 mT for DOC4, 60 mT for DOC5a, 75 mT for DOC 5b, 70 mT for DOC 6a, and 100 mT for DOC 6b. For samples DOC1, DOC2, DOC3a, DOC3b and DOC4, the applied direction of the ARM was directly in the -*z* direction. For samples DOC5b and DOC6b the direction of the applied ARM was in the +*z* direction. Overall, the direction of the acquired ARM is within 15% of the direction of applied field for all samples. Because of this, we chose not to apply an anisotropy correction to any of our samples.

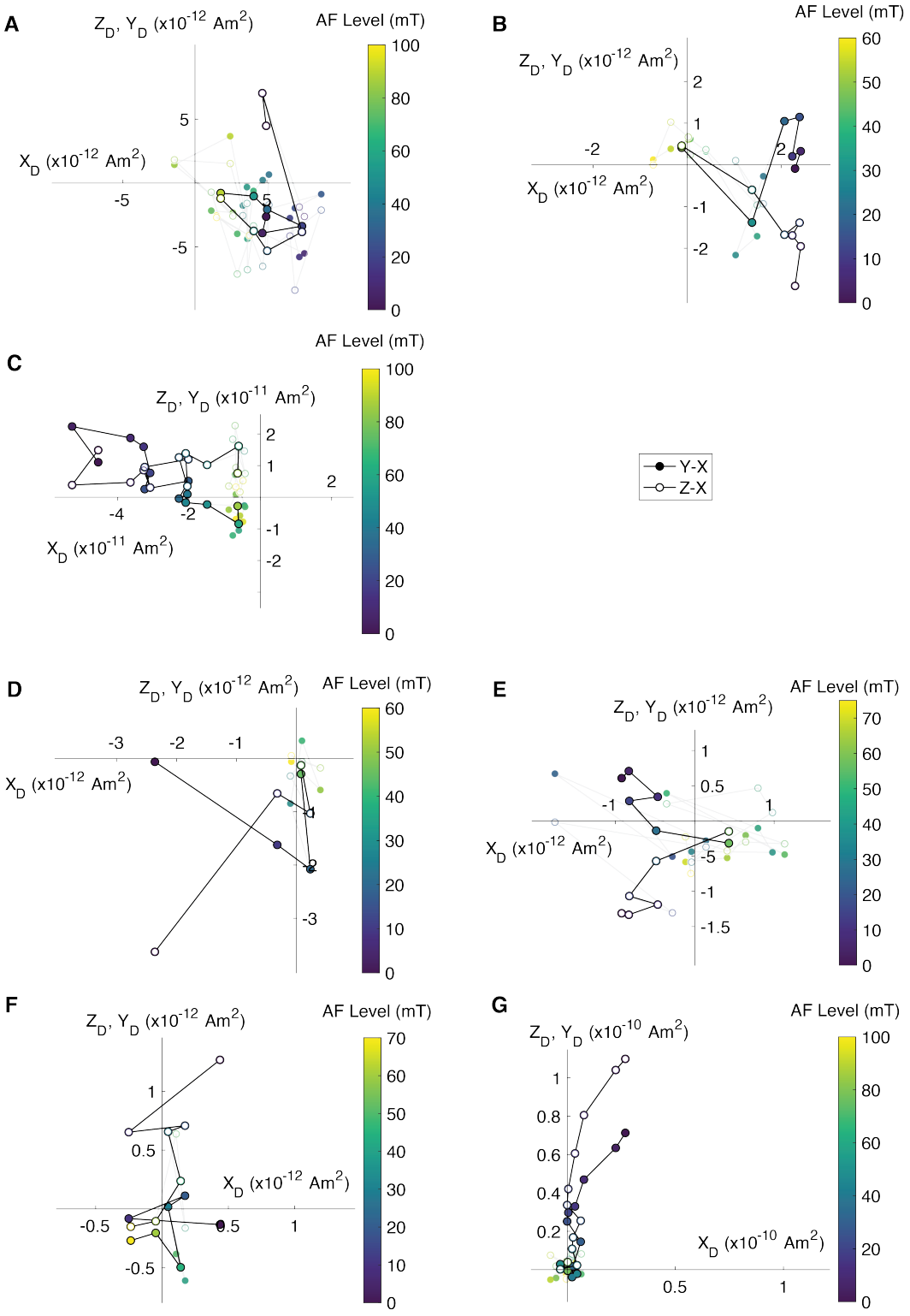

Fig. S3. AF demagnetization of dusty olivine chondrules from DOM 08006. (**A**) DOC3a. (**B**) DOC3b. (**C**) DOC4. (**D**) DOC5a. (**E**) DOC5b (**F**) DOC6a. (**G**) DOC6b. Shown are orthographic projections of the NRM vector endpoints. Closed symbols show the Y-X projection of the moment; open symbols show Z-X projection of the moment. Samples were oriented in the same coordinate system as the samples in Fig. 1C-D. Colorbar shows the AF levels of the steps. Opaque symbols denote datapoints averaged across multiple AF levels while semi-transparent symbols denote unaveraged data. Averaged levels are summarized in the Table S1.

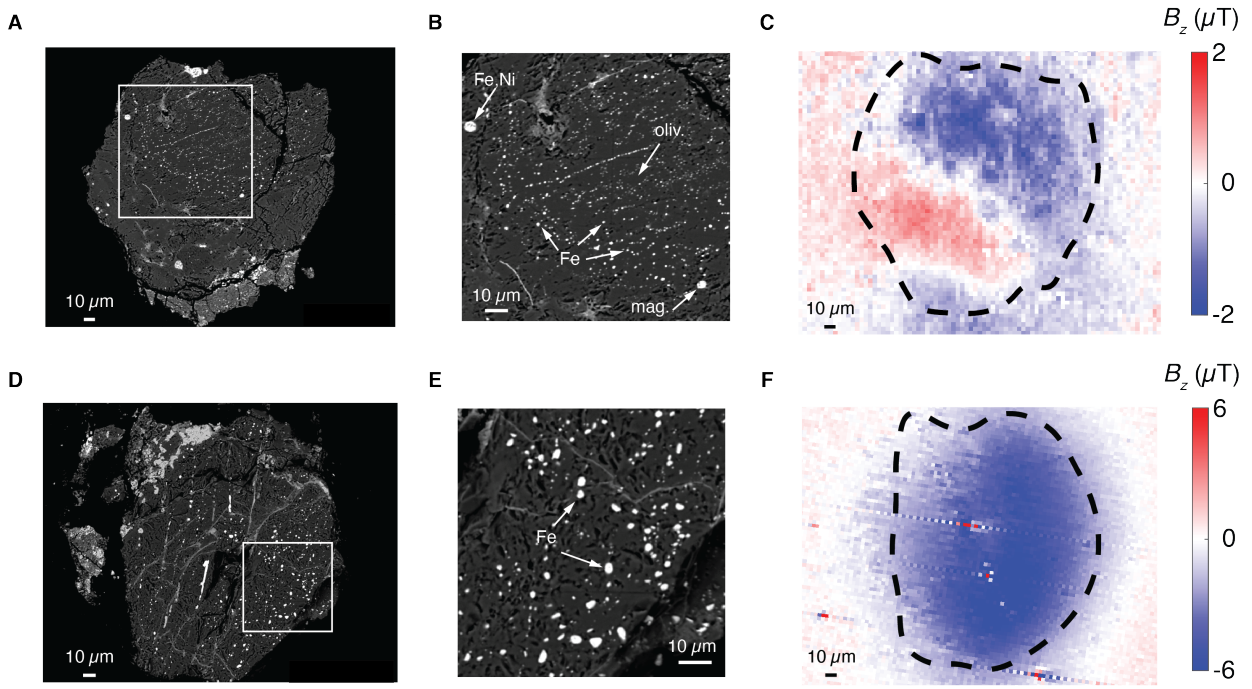

Fig. S4. BSE images, WDS analysis and QDM maps for samples DOC2 (A-C) and DOC6b (D-F). (A and D) BSE images with a white square showing the zoom in for (B) and (E). **(B and E)** Magnified view of the BSE images in (A) and (D). WDS analysis shows the presence of pure Fe in forsterite (oliv.) indicating that these samples are dusty olivine grains. We also observe the presence of Fe,Ni metal inclusions and a magnetite (mag.) inclusion in the sample. **(C and F)** QDM maps of the samples with dashed lines depicting the outline of the grains shown in (A) and (D). (C) QDM map showing the last step of the demagnetization of a 200 μT ARM. (F) QDM maps showing an ARM application (DC field 200 μT, AC field 100 mT) oriented in the into-the-page direction. The saturation points in the QDM map are artifacts from the diamond. In both maps, the magnetization originates from the region where the dusty olivine Fe grains are located.

5. Temporal or spatial variation?

To determine the probability that the measurements from the non-carbonaceous reservoir (*11*) and those obtained in this study from the carbonaceous reservoir reflect a temporal variation in the accretion rate, we conducted two numerical experiments using Monte Carlo simulations. Specifically, we sought to test the hypothesis that a single step change in the magnetic field and, by implication in the accretion rate, at some time t^* could explain the differences in accretion rates inferred from LL versus CO chondrules. A step change in the field is a limiting case because, if optimally timed, it would be more likely to produce a larger difference in average paleointensity between the two groups of chondrules than higher frequency field variations.

We started by fitting a normal distribution to the Al-Mg ages of the chondrules from Semarkona (LL3.0) and Y-81020 (CO3.0) (*12*). For Semarkona, we obtained a mean $\mu = 2.0$ Ma after CAI-formation and standard deviation $\sigma = 0.4$ Ma, while for Y-81020 we obtained a mean $\mu = 2.2$ Ma after CAI-formation and standard deviation $\sigma = 0.4$ Ma. For the first experiment, we randomly drew 5 ages [the number of chondrules used in ref. (*11*) to determine the mean LL dusty olivine chondrule paleointensity] from the normal distribution of LL ages to represent the LL chondrules from the non-carbonaceous reservoir. Similarly, we randomly drew 7 ages (the number

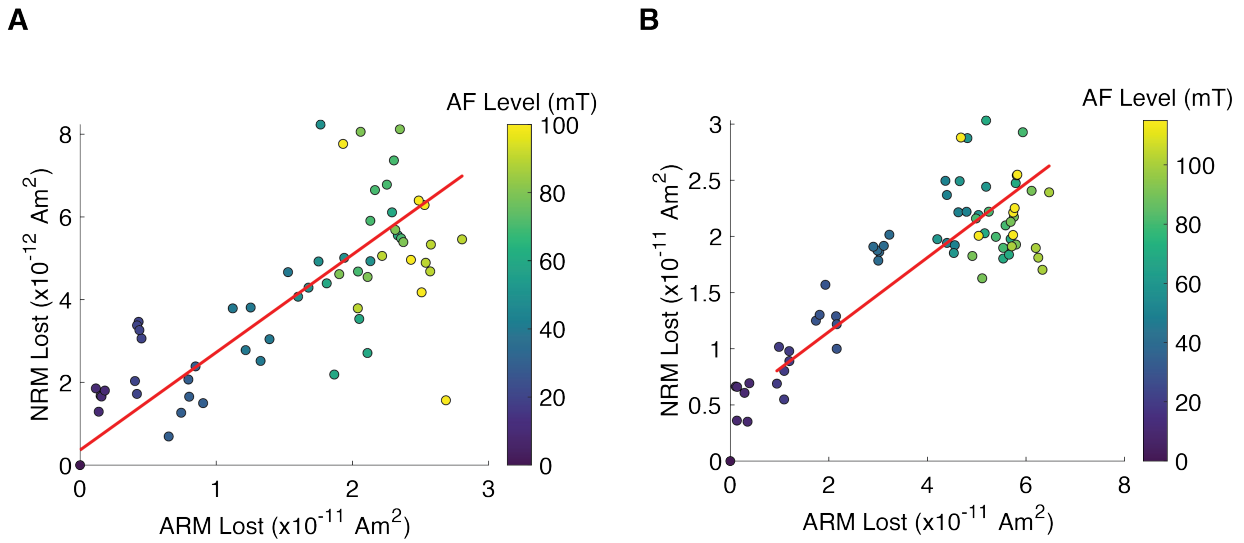

Fig. S5. Paleointensity experiments for ALHA 77307. Shown is NRM lost versus ARM lost during AF demagnetization of dusty olivine chondrules. (**A**) DOC1. (**B**) DOC2. Red line shows the least squares fit over the coercivity range used to calculate the paleointensity. Table S5 shows the paleointensity and the 95% confidence interval for the fit.

of chondrules used to determine the paleointensity in this study) from the normal distribution of CO ages to represent the chondrules we measured from the carbonaceous reservoir. The random sampling from the normal distribution used the function `normrnd` in MATLAB. We repeated this experiment for values of t^* between 1 and 3 Ma after CAI formation to span the range of chondrules ages. Because the LL and CO paleointensities support an aligned configuration between the rotation axis of the disk and the net vertical magnetic field (see main text), we used Eq. (3) from ref. (*10*) taking $f' = 10$ and $m = 10$ to calculate the accretion rates. Using the mean LL paleointensity of 54 μT and a formation region of 2 AU (3), and the mean CO paleointensity of 101 μT from this study with a formation region of 5 AU, we obtained accretion rates of 3.9×10^{-9} solar masses ($M_\odot$) year^{-1} and 1.3×10^{-7} $M_\odot$ year^{-1}, respectively. We took the calculated LL accretion rate as the low accretion rate value ($\dot{M}_{\rm low}$), while the calculated CO accretion rate was taken as the high accretion rate value ($\dot{M}_{\rm high}$). We identified two scenarios for the step change of the accretion rate: (1) the accretion rate increased at t^* and (2) the accretion rate decreased at t^*. If the randomly selected age was $< t^*$ for the increase/decrease case the low/high accretion rate was assigned. If the randomly selected age $> t^*$, for the increase/decrease case a high/low accretion rate was assigned. We then averaged the accretion rate values for each reservoir and for each case. This experiment was conducted 100,000 times. For each scenario, we calculated the ratio of the mean accretion rate in the carbonaceous reservoir and the mean accretion rate in the non-carbonaceous reservoir. Experiments that had this ratio $\geq \dot{M}_{\rm high}/\dot{M}_{\rm low} = 1.3\times10^{-7}\,M_\odot$ year^{-1}/$3.9\times10^{-9}\,M_\odot$ year^{-1} ~33 were taken as realizations supporting a time-varying accretion rate in the first 3 Ma after CAI formation. We found that the highest probability of such scenario is 0.37% (Table S6; Figs. S8 and S10A-B).

We also took a more conservative approach in which we used the +1σ upper bound on the LL paleointensities (*11*) of 54 + 21/2 = 64.5 μT to calculate $\dot{M}_{\rm low}$ and the mean -1σ lower bound on the CO paleointensities (this study) of 101 – 48/2 = 77 μT to calculate $\dot{M}_{\rm high}$. For this case, we

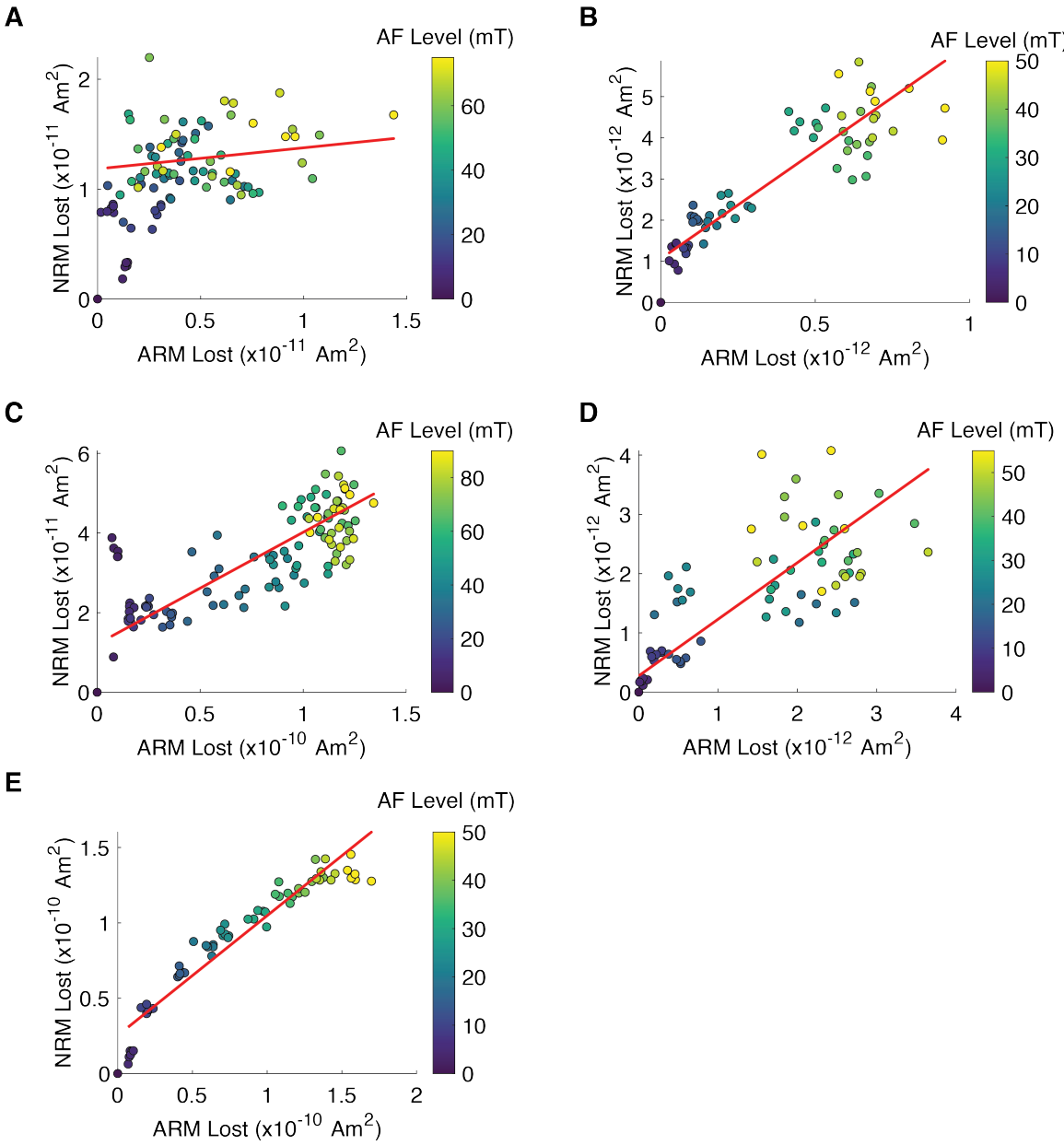

Fig. S6. Paleointensity experiments for DOM 08006. Shown are NRM lost versus ARM lost during AF demagnetization of dusty olivine chondrules. (**A**) DOC3a. (**B**) DOC3b. (**C**) DOC4. (**D**) DOC5b. (**E**) DOC6b. Red line shows the least squares fit over the coercivity range used to calculate the paleointensity. Table S5 shows the paleointensity and the 95% confidence interval for the fit.

also assumed that both samples formed at 3 AU. Using the same equations as before, we obtained $\dot{M}_{\mathrm{low}} = 1.5{\times}10^{-8}\ M_{\odot}$ year^{-1} and $\dot{M}_{\mathrm{high}} = 2.2{\times}10^{-8}$ s $M_{\odot}$ year^{-1}. Similarly to the previous analysis, experiments that had the ratio between the mean accretion rate in the carbonaceous reservoir to the mean accretion rate in the non-carbonaceous reservoir $\geq \dot{M}_{\mathrm{high}}/\dot{M}_{low} = 2.2{\times}10^{-8}\ M_{\odot}$ year^{-1}/$1.5{\times}10^{-8}\ M_{\odot}$ year^{-1} ~1.46, were taken as realizations that would satisfy that the measured magnetic fields

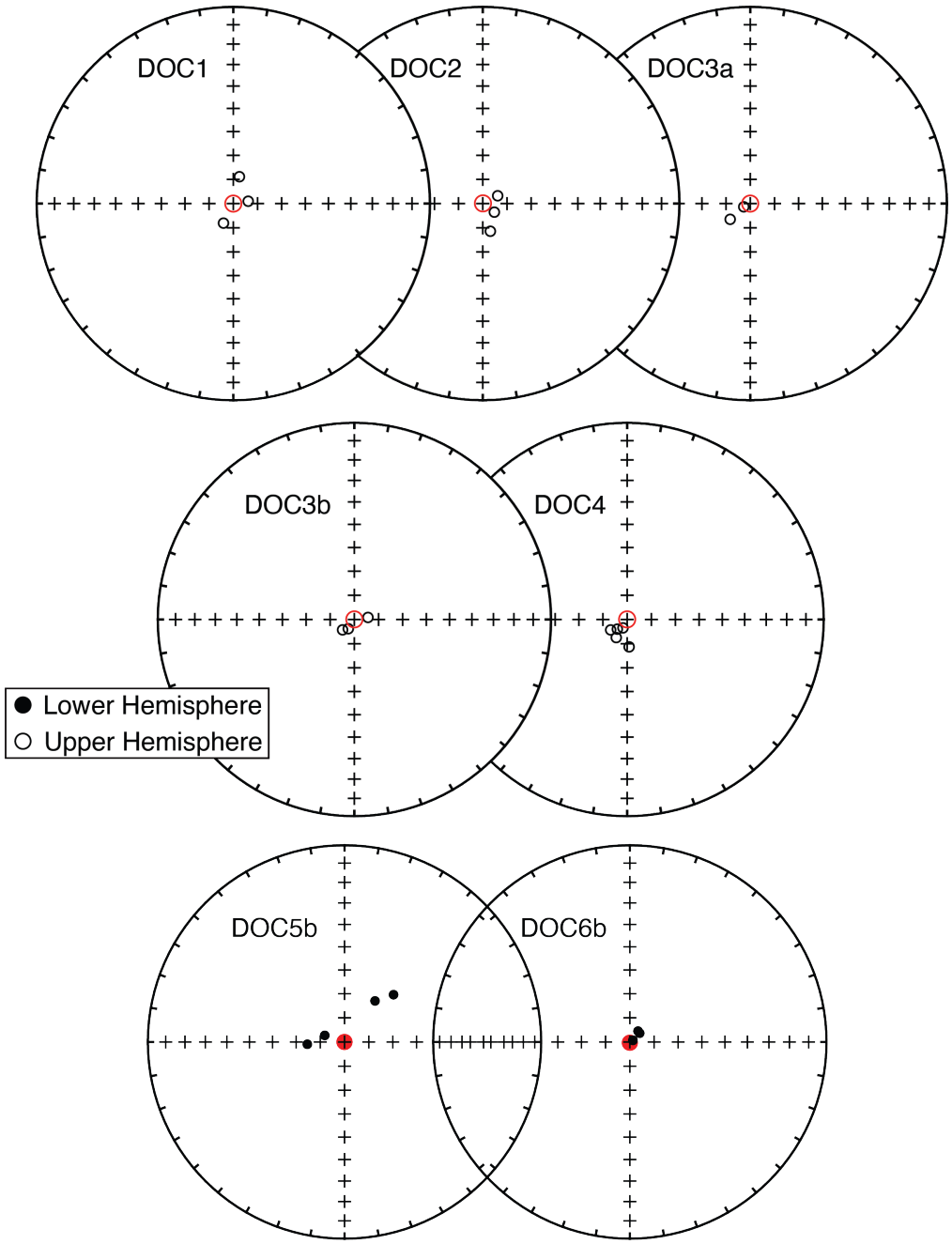

Fig. S7. ARM acquisition by dusty olivine chondrules from ALHA 77307 and DOM 08006. Each datapoint shows the ARM direction with a bias field of 200 μT and AF indicated in section 6. Red circles show the direction of the applied bias magnetic field. We also subtracted the last NRM datapoint from the ARM acquisition.

[from ref. (*11*) and this study] support a time varying accretion rate in the first 3 Ma after CAI formation. The highest probability of such scenario was 0.40% (Table S6; Figs. S9 and S10C-D).

Finally, we also conducted Monte Carlo simulations using recently reported Al-Mg ages with smaller measurement spot sizes for chondrules from Semarkona (*63*, *64*) and chondrules from the carbonaceous reservoir (Acfer 094 and Kaba) (*65*, *66*). Note that some of these measurements

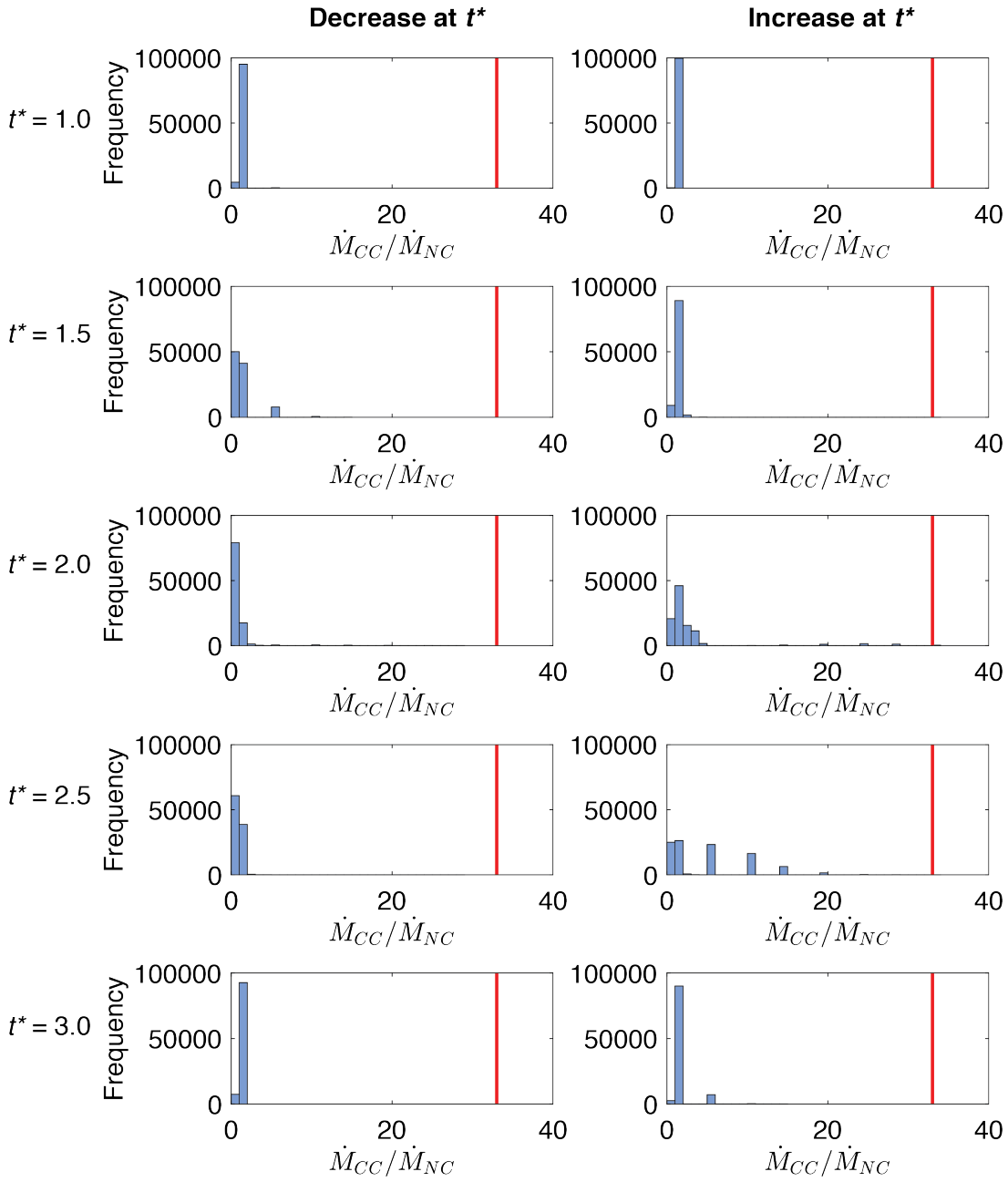

Fig. S8. Monte Carlo simulations assessing the possibility that a temporal change in accretion rates can explain the differences in accretion rates inferred from CO and LL paleointensities. Each plot shows a histogram of the mean accretion rate in the carbonaceous reservoir ($\dot{M}_{\mathrm{CC}}$) over the mean accretion rate in the non-carbonaceous reservoir ($\dot{M}_{\mathrm{NC}}$). Left column shows simulations for an accretion rate that decreases at t^*. Right column shows simulations for an accretion rate that increases at t^*. From top to bottom are simulations for different choices of t^*. Red line indicates the threshold ratio of 33.

for Y-81020 have only appeared in abstract form. These recent Al-Mg measurements suggest that the formation time of chondrules in the non-carbonaceous and the carbonaceous reservoir were not contemporaneous and that previously reported measurements (*12*) were affected by

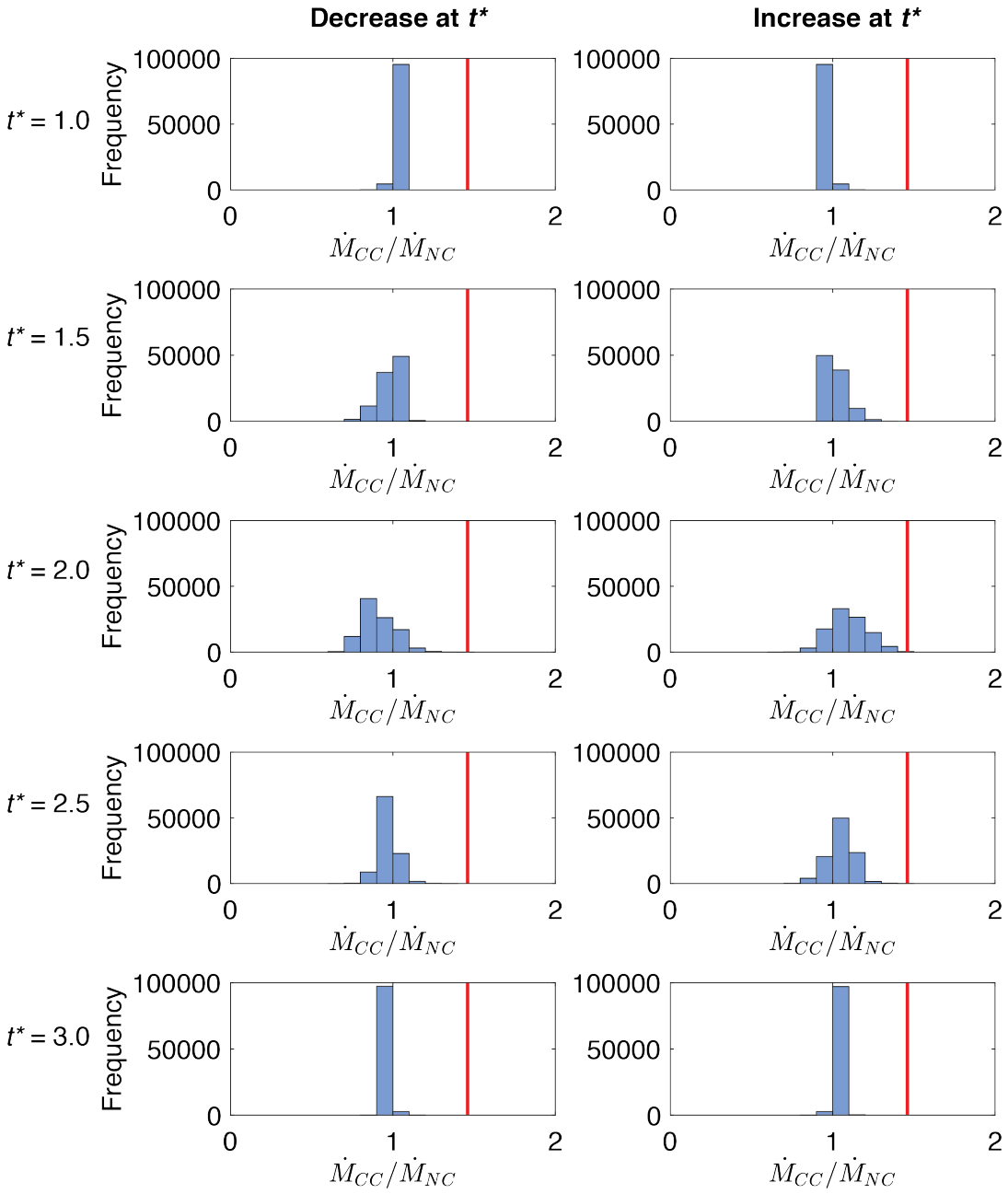

Fig. S9. Monte Carlo simulations assessing the possibility that a temporal change in accretion rates can explain the differences in accretion rates inferred from CO and LL paleointensities. Each plot shows a histogram of the mean accretion rate in the carbonaceous reservoir ($\dot{M}_{\mathrm{CC}}$) over the mean accretion rate in the non-carbonaceous reservoir ($\dot{M}_{\mathrm{NC}}$). Left column shows simulations for an accretion rate that decreases at t^*. Right column shows simulations for an accretion rate that increases at t^*. From top to bottom are simulations for different choices of t^*. Red line indicates the threshold ratio of 1.46.

disturbances of the Al-Mg system due to parent-body metamorphism (*63*). For the non-carbonaceous reservoir, we used a mean of μ = 2.0 Ma after CAI-formation and a standard deviation of σ = 0.1 Ma, while for the carbonaceous reservoir we used a mean of μ = 2.4 Ma after

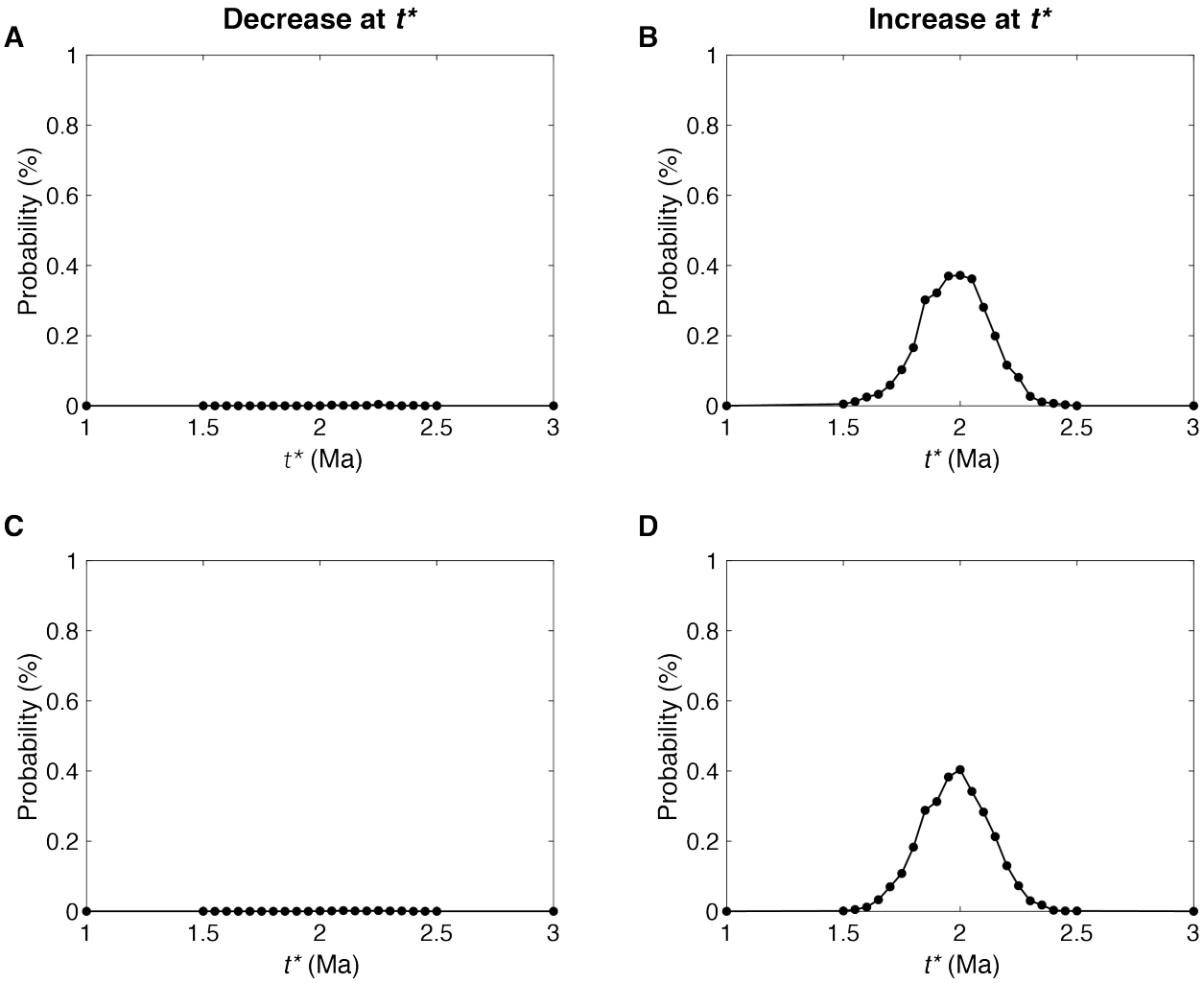

Fig. S10. Probabilities from Monte Carlo simulations. Each datapoint represents the percentage of cases from 100,000 simulations in which our measurements represent temporal variations. t^* represents the time that the accretion rate (left) decreases and (right) increases, assuming ages for the two reservoirs reported in ref. (11). **(A, B)** Assumes a threshold ratio of 33. **(C, D)** Assumes a threshold ratio of 1.46.

CAI-formation and a standard deviation of σ = 0.2 Ma. Experiments that had the ratio between the mean accretion rate in the carbonaceous reservoir to the mean accretion rate in the non-carbonaceous reservoir $\geq \dot{M}_{\mathrm{high}}/\dot{M}_{low}$ ~33 were taken as realizations that would satisfy that the measured magnetic fields [from ref. (*11*) and this study] support a time varying accretion rate in the first 3 Ma after CAI formation. The highest probability of such scenario was 32.7% (Table S6; Fig. S11A-B). We also assumed a ratio $\geq \dot{M}_{\mathrm{high}}/\dot{M}_{\mathrm{low}}$ ~1.46 and the highest probability in this case was 32.4% (Table S6; Figs. S11C-D).

Overall, our simulations show that it is unlikely, even for the most conservative cases, that the samples obtained for this study and from previous measurements have recorded magnetic fields that are consistent with a temporal variation in solar accretion rate.

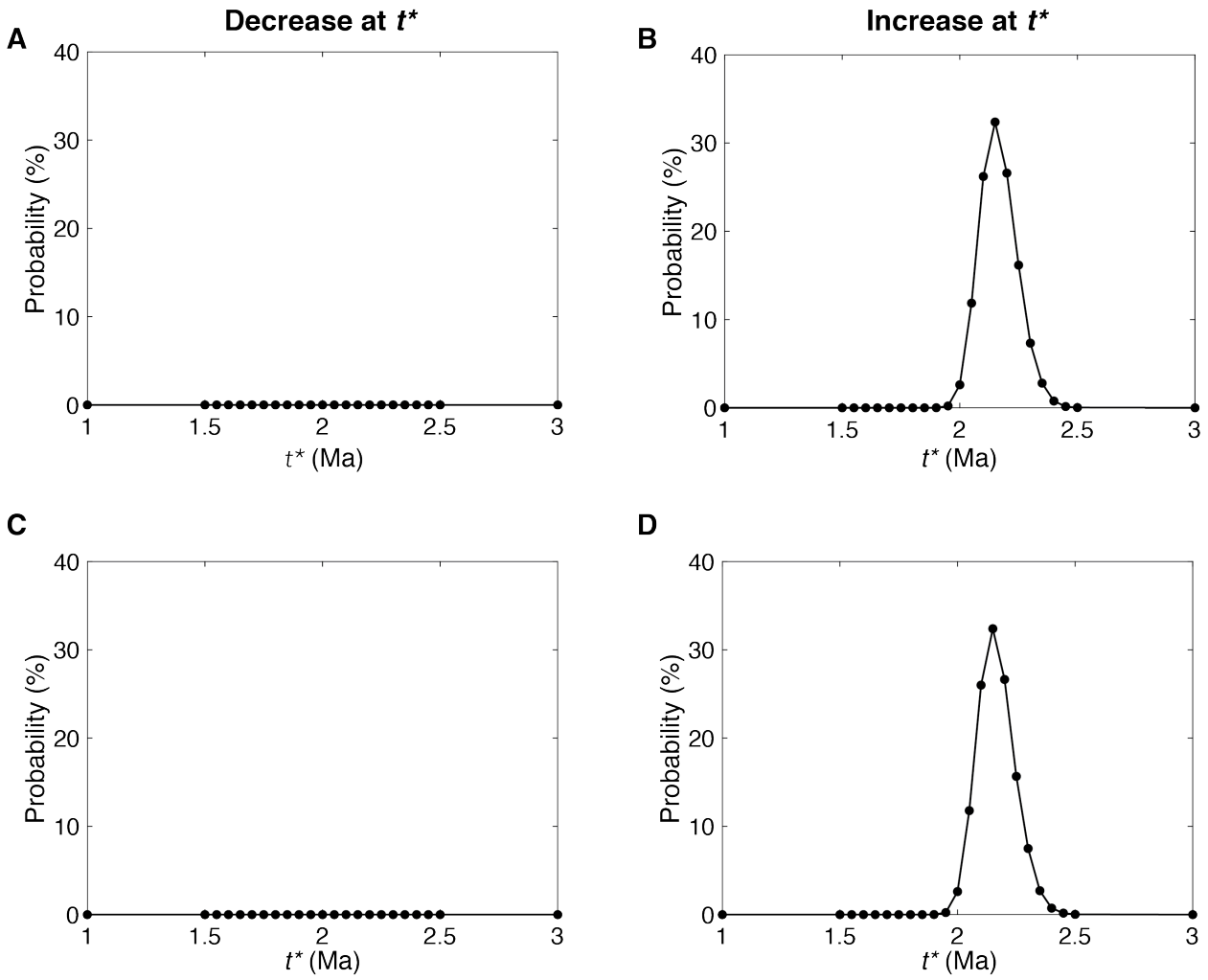

Fig. S11. Probabilities from Monte Carlo simulations. Each datapoint represents the percentage of cases from 100,000 simulations in which our measurements represent temporal variations. *t** represents the time that the accretion rate (left) decreases and (right) increases, assuming ages for the two reservoirs reported in refs. (*57-60*). **(A, B)** Assumes a threshold ratio of 33. **(C, D)** Assumes a threshold ratio of 1.46.

Sample	Meteorite	Orientation Measured	Distance to fusion crust (mm)	NRM (Am^2)	Averages (mT)	Component	Range (mT)	N	MAD not anc. (°)	DANG (°)	Anc.?	Dec. (°)	Inc. (°)	MAD (°)
DOC1	ALHA	N	3.3	5.6E-12	5-20; 40-90; 100-145	HC	0-160	8	28.1	9.1	Y	9.2	21.5	16
DOC2	ALHA	S	5.8	2.3E-11	50-145; 145-410	LC	0-10	3	11.9	-	N	197.4	-83.1	11.9
						HC	15-272	8	16.5	4.1	Y	76.5	-27.9	9.9
DOC3a	DOM	T	7	7.2E-12	10-30; 40-65; 80-100	LC	0-20	3	6.5	-	N	266.8	-75.1	6.5
						HC	20-90	11	23.1	8	Y	112.1	34.7	9.6
DOC3b	DOM	T	7	3.7E-12	25-35, 40-60	LC	0-5	2	0	-	N	195.7	65.6	0
						HC	5-50	6	32.1	14	Y	77.9	35.2	18.7
DOC4	DOM	B	7.5	4.9E-11	55-65; 70-100	LC	0-5	2	0	-	N	147.1	-39.3	0
						HC	5-85	12	16.8	37.7	N	305.1	10	16.8
DOC5a	DOM	B	8	4.3E-12	30-60	HC	0-45	4	23.3	53.9	N	297.5	48.6	23.3
DOC5b	DOM	B	8	1.7E-12	20-35; 35-75	HC	0-55	6	15.4	23.9	N	310.8	36.9	15.4
DOC6a	DOM	T	6	1.3E-12	40-50	HC	0-70	7	24.1	32.2	Y	59.9	-67.8	24.1
DOC6b	DOM	T	6	1.3E-10	55-100	HC	0-77.5	12	7.4	4	Y	15.7	-57.4	5.5

Table S1. Summary of PCAs of the dusty olivine chondrules. The first column lists the sample name, the second column lists the meteorite ("ALHA" for ALHA 77307 and "DOM" for DOM 08006), the third column lists the orientation of the sample as measured in magnetometer coordinates following the diagram from Fig. S1, the fourth column lists the magnetic moment of the NRM in Am^2, the fifth column lists the steps that were averaged in mT, the sixth column lists the name of the component ("LC" for low coercivity and "HC" for high coercivity), the seventh column lists the range used to calculate the fit in mT, the eighth column lists the number of steps used to calculate the component, the ninth column lists the maximum angle deviation (MAD) for the non-anchored component, the tenth column lists the deviation angle (DANG) for the component, the eleventh column denotes whether the component is anchored ("Y" for yes and "N" for no), the twelfth through fourteenth columns list the declination, inclination and MAD for the component.

Meteorite	*N*	Length of the resultant of the vectors (*R*)	Critical length of the resultant of the vectors (R_0)
ALHA 77307	2	1.51	1.85
DOM 08006	4	1.48	3.02

Table S2. Summary of the Watson's randomness test for each meteorite. The first column lists the meteorite name, the second column shows the number of chondrules, the third column shows the calculated length of the results of the vectors, the fourth column shows the critical length of the resultant of the vectors for a 95% confidence interval.

Sample	Analysis	SiO_2	TiO_2	Al_2O_3	Cr_2O_3	FeO	MnO	MgO	CaO	Na_2O	NiO	ZnO	Total
DOC2	Forsterite	42.52	0.00	0.02	0.40	0.87	0.30	56.64	0.14	-	-	-	100.89
	Forsterite	42.79	0.02	0.02	0.40	1.09	0.19	56.00	0.11	-	-	-	100.63
	Forsterite	42.55	0.01	0.02	0.38	0.72	0.22	56.18	0.24	-	-	-	100.33
	Forsterite	42.62	0.02	0.05	0.37	0.73	0.25	56.62	0.16	-	-	-	100.81
	Forsterite	42.58	0.01	0.03	0.32	0.69	0.24	56.54	0.14	-	-	-	100.55
	Magnetite	1.48	0.00	0.08	2.65	82.03	0.06	0.62	0.12	-	2.57	0.00	89.61
DOC6b	Forsterite	41.45	0.03	0.02	0.52	1.38	0.29	56.42	0.18	-	-	-	100.28
	Forsterite	41.67	0.00	0.03	0.49	1.84	0.28	57.30	0.18	-	-	-	101.79
	Forsterite	41.93	0.00	0.02	0.43	2.26	0.24	56.08	0.19	-	-	-	101.16
	Forsterite	41.88	0.00	0.02	0.50	1.40	0.19	56.50	0.20	-	-	-	100.70
	Forsterite	42.73	0.00	0.04	0.45	1.45	0.22	56.15	0.20	-	-	-	101.24
	Magnetite	0.93	0.00	0.02	0.21	88.11	0.04	1.30	0.01		2.34	0.00	92.97

Table S3. Summary of WDS analysis of forsterite and magnetite conducted in samples DOC2 and DOC6b. The first column shows the sample name, the second column shows the interpretation of the mineral, the third through thirteenth columns show the concentration of each element (weight percent), and the fourteenth column shows the sum of the percentages.

Sample	Analyses	Fe	Ni	Cr	Mn	P	S	O	Total
DOC2	Fe	93.64	0.06	0.91	0.05	0.03	0.03	3.55	98.26
	Fe	94.13	0.06	1.05	0.01	0.02	0.00	2.89	98.17
	Fe	93.36	0.06	1.21	0.11	0.03	0.02	4.18	98.97
	Fe,Ni	68.12	20.35	1.11	0.00	0.46	0.75	9.94	100.73
	Fe,Ni	77.82	4.59	0.66	0.04	0.45	0.45	11.43	95.44
DOC6b	Fe	97.57	0.03	0.29	0.00	0.02	0.00	0.36	98.27
	Fe	97.27	0.02	0.25	0.03	0.02	0.01	0.62	98.21
	Fe	97.16	0.04	0.30	0.05	0.03	0.02	1.36	98.95

Table S4. Summary of WDS analysis of metal grains in samples DOC2 and DOC6b. The first column shows the sample name, the second column shows the interpretation of the mineral, the third through seventh columns show the concentration of each element (weight percent), and the eighth column shows the sum of the percentages.

Sample	Meteorite	Range (mT)	*N*	*ρ*	Fit Type	Paleointensity (*μ*T)	95% Confidence Interval (*μ*T)
DOC1	ALHA	0-100	61	0.7	RMA	25.3	4.8
DOC2	ALHA	20-115	60	0.8	RMA	35.3	6.4
					ALHA mean	**30**	
					95% confidence Interval	**10**	
DOC3a	DOM	20-75	72	0.2	OLS	20.5	26.3
DOC3b	DOM	5-50	60	0.9	RMA	55.9	6.9
DOC4	DOM	5-90	108	0.8	RMA	30	3.9
DOC5b	DOM	5-55	50	0.7	RMA	102.1	19.2
DOC6b	DOM	5-50	60	1	RMA	85.1	6.7
					DOM mean	**59**	
					95% confidence Interval	**31**	
					Mean Paleointensity	**51**	
					95% confidence Interval	**24**	
					Corrected Mean Paleointensity	**101**	
					95% confidence Interval	**48**	

Table S5. Summary of the statistics of the paleointensity of the dusty olivine chondrules. The first column lists the sample name, the second column lists the meteorite ("ALHA" for ALHA 77307 and "DOM" for DOM 08006), the third column lists the AF range used for the fit to in mT, the fourth lists the number of measurements used in the fit to ΔNRM versus ΔARM, the fifth column lists the correlation coefficient associated with fits, the sixth column lists the fit type ("RMA" for reduced major axis and "OLS" for ordinary least squares), the seventh column lists the paleointensity calculated from the fit in μT, and the eighth column lists the 95% confidence interval of the fit. For each meteorite, we also show the mean and the 95% confidence interval. At the bottom, we list the grand mean and the grand mean corrected for chondrule spin along with their 95% confidence intervals.

	Probability of Temporal Variation in Accretion Rate				
Threshold ≥ 33 R_{NC} = 2 AU, R_{CC} = 5 AU Ages from ref. (11)	**Time of field change (*t**, Ma after CAI formation)**				
	1.0	**1.5**	**2.0**	**2.5**	**3.0**
Field decreases at *t**	0%	0%	0%	0%	0%
Field increases at *t**	0%	0.005%	0.372%	0%	0%
Threshold ≥ 1.46 R_{NC} = R_{CC} = 3 AU Ages from ref. (11)	**Time of field change (*t**, Ma after CAI formation)**				
	1.0	**1.5**	**2.0**	**2.5**	**3.0**
Field decreases at *t**	0%	0%	0.001%	0%	0%
Field increases at *t**	0%	0.001%	0.404%	0.001%	0%
Threshold ≥ 33 R_{NC} = R_{CC} = 3 AU Ages from refs. (*57-60*)	**Time of field change (*t**, Ma after CAI formation)**				
	1.0	**1.5**	**2.15**	**2.5**	**3.0**
Field decreases at *t**	0%	0%	0%	0%	0%
Field increases at *t**	0%	0%	32.372%	0.026%	0%
Threshold ≥ 1.46 R_{NC} = R_{CC} = 3 AU Ages from refs. (*57-60*)	**Time of field change (*t**, Ma after CAI formation)**				
	1.0	**1.5**	**2.15**	**2.5**	**3.0**
Field decreases at *t**	0%	0%	0%	0%	0%
Field increases at *t**	0%	0%	32.388%	0.003%	0%

Table S6. Summary of selected Monte Carlo simulations used to the determine the probability that the measurements considered in this study represent a time variation in the accretion rate. Shown are the probabilities for two distinct thresholds values, two distinct locations for the carbonaceous and non-carbonaceous reservoirs, and two distinct set of ages. The two distinct thresholds (see Section 5) represent the ratio between the accretion rate in the carbonaceous reservoir and the accretion rate in the non-carbonaceous reservoir. Columns two through six show the probabilities for the nebular field changing at a time t^*, where t^* = 1, 1.5, 2, 2.5 and 3.0 Ma after CAI formation, respectively. The first row of each table shows the probability for the cases in which the accretion rate increases at t^*, while the second row of each table shows the probability for the cases in which the accretion rate decreases at t^*.

REFERENCES AND NOTES

1. S. M. Andrews, Observations of protoplanetary disk structures. *Annu. Rev. Astron. Astrophys.* **58**, 483–528 (2020).
2. T. S. Kruijer, T. Kleine, L. E. Borg, The great isotopic dichotomy of the early solar system. *Nat. Astron.* **4**, 32–40 (2020).
3. E. R. D. Scott, A. N. Krot, I. S. Sanders, Isotopic dichotomy among meteorites and its bearing on the protoplanetary disk. *Astrophys. J.* **854**, 164 (2018).
4. T. Kleine, G. Budde, C. Burkhardt, T. S. Kruijer, E. A. Worsham, A. Morbidelli, F. Nimmo, The non-carbonaceous–carbonaceous meteorite dichotomy. *Space Sci. Rev.* **216**, 55 (2020).
5. R. Brasser, S. J. Mojzsis, The partitioning of the inner and outer solar system by a structured protoplanetary disk. *Nat. Astron.* **4**, 492–499 (2020).
6. T. Lichtenberg, J. Drążkowska, M. Schönbächler, G. J. Golabek, T. O. Hands, Bifurcation of planetary building blocks during Solar System formation. *Science*. **371**, 365–370 (2021).
7. X.-N. Bai, J. Goodman, Heat and dust in active layers of protostellar disks. *Astrophys. J.* **701**, 737–755 (2009).
8. X.-N. Bai, Global simulations of the inner regions of protoplanetary disks with comprehensive disk microphysics. *Astrophys. J.* **845**, 75 (2017).
9. N. J. Turner, S. Fromang, C. Gammie, H. Klahr, G. Lesur, M. Wardle, X.-N. Bai, in *Protostars and Planets VI*, H. Beuther, R. S. Klessen, C. P. Dullemond, T. K. Henning, Eds. (University of Arizona Press, 2014), pp. 411–432.
10. B. P. Weiss, X.-N. Bai, R. R. Fu, History of the solar nebula from meteorite paleomagnetism. *Sci. Adv.* **7**, eaba5967 (2021).
11. R. R. Fu, B. P. Weiss, E. A. Lima, R. J. Harrison, X.N. Bai, S. J. Desch, D. S. Ebel, C. Suavet, H. Wang, D. Glenn, D. le Sage, T. Kasama, R. L. Walsworth, A. T. Kuan, Solar nebula magnetic fields recorded in the Semarkona meteorite. *Science* **346**, 1089–1092 (2014).
12. N. T. Kita, T. Ushikubo, Evolution of protoplanetary disk inferred from ^{26}Al chronology of individual chondrules. *Meteorit. Planet. Sci.* **47**, 1108–1119 (2011).
13. C. Cournède, J. Gattacceca, M. Gounelle, P. Rochette, B. P. Weiss, B. Zanda, An early solar system magnetic field recorded in CM chondrites. *Earth Planet. Sci. Lett.* **410**, 62–74 (2015).
14. R. R. Fu, P. Kehayias, B. P. Weiss, D. L. Schrader, X.-N. Bai, J. B. Simon, Weak magnetic fields in the outer solar nebula recorded in CR chondrites. *J. Geophys. Res.*, **125**, e2019JE006260 (2020).

15. R. R. Fu, M. W. R. Volk, D. Bilardello, D. Libourel, G. R. J. Lesur, O. Ben Dor, The fine-scale magnetic history of the Allende meteorite: implications for the structure of the solar nebula. *AGU Adv.* **2**, e2021AV000486 (2021).
16. D. L. Schrader, K. Nagashima, A. N. Krot, R. C. Ogliore, Q.Z. Yin, Y. Amelin, C. H. Stirling, A. Kaltenbach, Distribution of ^{26}Al in the CR chondrite chondrule-forming region of the protoplanetary disk. *Geochim. Cosmochim. Acta* **201**, 275–302 (2017).
17. L. Carporzen, B. P. Weiss, L. T. Elkins-Tanton, D. L. Shuster, D. S. Ebel, J. Gattacceca, Magnetic evidence for a partially differentiated carbonaceous chondrite parent body. *Proc. Natl. Acad. Sci. U.S.A.* **108**, 6386–6389 (2011).
18. H. Wang, B. P. Weiss, X.-N. Bai, B. G. Downey, J. Wang, J. Wang, C. Suavet, R. R. Fu, M. E. Zucolotto, Lifetime of the solar nebula constrained by meteorite paleomagnetism. *Science* **355**, 623–627 (2017).
19. L. Bonal, M. Bourot-Denise, E. Quirico, G. Montagnac, E. Lewin, Organic matter and metamorphic history of CO chondrites. *Geochim. Cosmochim. Acta* **71**, 1605–1623 (2007).
20. J. Davidson, C. M. O'D. Alexander, R. M. Stroud, H. Busemann, L. R. Nittler, Mineralogy and petrology of Dominion Range 08006: A very primitive CO3 carbonaceous chondrite. *Geochim. Cosmochim. Acta* **265**, 259–278 (2019).
21. C. M. O'D. Alexander, R. C. Greenwood, R. Bowden, J. M. Gibson, K. T. Howard, I. A. Franchi, A mutli-technique search for the most primitive CO chondrites. *Geochim. Cosmochim. Acta* **221**, 406–420 (2018).
22. E. R. D. Scott, K. Keil, D. Stöffler, Shock metamorphism of carbonaceous chondrites. *Geochim. Cosmochim. Acta* **56**, 4281–4293 (1992).
23. C. M. O'D. Alexander, M. Fogel, H. Yabuta, G. D. Cody, The origin and evolution of chondrites recorded in the elemental and isotopic compositions of their macromolecular organic matter. *Geochim. Cosmochim. Acta* **71**, 4380–4403 (2007).
24. J. Shah, W. Williams, T. P. Almeida, L. Nagy, A. R. Muxworthy, A. Kovács, M. A. Valdez-Grijalva, K. Fabian, S. S. Russell, M. J. Genge, The oldest magnetic record in our solar system identified using nanometric imaging and numerical modeling. *Nat. Commun.* **9**, 1–6 (2018).
25. J. F. Einsle, R. J. Harrison, T. Kasama, P. Ó. Conbhuí, K. Fabian, W. Williams, L. Woodland, R. R. Fu, B. P. Weiss, P. A. Midgley, Multi-scale three-dimensional characterization of iron particles in

dusty olivine: Implications for paleomagnetism of chondritic meteorites. *Am. Mineral.* **101**, 2070–2084 (2016).

26. S.-C. L. L. Lappe, N. S. Church, T. Kasama, A. B. da Silva Fanta, G. Bromiley, R. E. Dunin-Borkowski, J. M. Feinberg, S. Russell, R. J. Harrison, Mineral magnetism of dusty olivine: A credible recorder of pre-accretionary remanence. *Geochem. Geophys. Geosyst.* **12**, Q12Z35 (2011).
27. S.-C. L. L. Lappe, J. M. Feinberg, A. Muxworthy, R. J. Harrison, Comparison and calibration of nonheating paleointensity methods : A case study using dusty olivine. *Geochem. Geophys. Geosyst.* **14**, 2143–2158 (2013).
28. E. R. D. Scott, A. N. Krot, in *Treatise on Geochemistry*, vol. 2 of *Planets, Asteroids, Comets, and the Solar System*, H. D. Holland, K. K. Turekian, Eds. (Elsevier Science, 2013), pp. 66–137.
29. S. J. Desch, M. A. Morris, H. C. Connolly Jr., A. P. Boss, The importance of experiments: Constraints on chondrule formation models. *Meteorit. Planet. Sci.* **47**, 1139–1156 (2012).
30. S. J. Desch, M. A. Morris, H. C. Connolly Jr., A. P. Boss, A critical examination of the X-wind model for chondrule and calcium-rich, aluminum-rich inclusion formation and radionuclide production. *Astrophys. J.* **725**, 692–711 (2010).
31. Recent high-precision Al-Mg ages of LL chondrules support a shorter formation interval than previous Al-Mg ages. See Supplementary Text for more information.
32. B. P. Weiss, E. A. Lima, L. E. Fong, F. J. Baudenbacher, Paleomagnetic analysis using SQUID microscopy. *J. Geophys. Res.* **112**, B09105 (2007).
33. L. Nagy, W. Williams, L. Tauxe, A. R. Muxworthy, I. Ferreira, Thermomagnetic recording fidelity of nanometer-sized iron and implications for planetary magnetism. *Proc. Natl. Acad. Sci. U.S.A.* **116**, 1984–1991 (2019).
34. G. S. Watson, A test for randomness of directions. *Geophys. J. Int.* **7**, 160–161 (1956).
35. S. M. Tikoo, B. P. Weiss, W. S. Cassata, D. L. Shuster, J. Gattacceca, E. A. Lima, C. Suavet, F. Nimmo, M. D. Fuller, Decline of the lunar core dynamo. *Earth Planet. Sci. Lett.* **404**, 89–97 (2014).
36. L. Hartmann, N. Calvet, E. Gullbring, P. D'Alessio, Accretion and the evolution of T Tauri disks. *Astrophys. J.* **495**, 385–400 (1998).
37. L. Hartmann, G. Herczeg, N. Calvet, Accretion onto pre-main-sequence stars. *Annu. Rev. Astron. Astrophys.* **54**, 135–180 (2016).

38. S. K. Atreya, A. Crida, T. Guillot, J. I. Lunine, N. Madhusudhan, O. Mousis, in *Saturn in the 21st Century*, K. H. Baines, F. M. Flasar, N. Krupp, T. Stallard, Eds. (Cambridge Univ. Press, 2018), pp. 5–43.
39. C. J. Clarke, A. Gendrin, M. Sotomayor, The dispersal of circumstellar discs: The role of the ultraviolet switch. *Mon. Not. R. Astron. Soc.* **328**, 485–491 (2001).
40. J. E. Owen, C. J. Clarke, B. Ercolano, On the theory of disc photoevaporation. *Mon. Not. R. Astron. Soc.* **422**, 1880–1901 (2012).
41. G. Picogna, B. Ercolano, J. E. Owen, M. L. Weber, The dispersal of protoplanetary discs – I. A new generation of X-ray photoevaporation models. *Mon. Not. R. Astron. Soc.* **487**, 691–701 (2019).
42. L. Wang, X.-N. Bai, J. Goodman, Global simulations of protoplanetary disk outflows with coupled non-ideal magnetohydrodynamics and consistent thermochemistry. *Astrophys. J.* **874**, 90 (2019).
43. X.-N. Bai, Toward a global evolutionary model of protoplanetary disks. *Astrophys. J.* **821**, 80 (2016).
44. T. K. Suzuki, M. Ogihara, A. Morbidelli, A. Crida, T. Guillot, Evolution of protoplanetary discs with magnetically driven disc winds. *Astron. Astrophys.* **596**, A74 (2016).
45. G. P. Rosotti, B. Ercolano, J. E. Owen, P. J. Armitage, The interplay between x-ray photoevaporation and planet formation. *Mon. Not. R. Astron. Soc.* **430**, 1392–1401 (2013).
46. J. L. Kirschvink, R. E. Kopp, T. D. Raub, C. T. Baumgartner, J. W. Holt, Rapid, precise, and high-sensitivity acquisition of paleomagnetic and rock-magnetic data: Development of a low-noise automatic sample changing system for superconducting rock magnetometers. *Geochem. Geophys. Geosyst.* **9**, Q05Y01 (2008),.
47. A. Stephenson, Three-axis static field demagnetization of rocks and the identification of natural remanent magnetization, gyroremanent magnetization, and anisotropy. *J. Geoph. Res.* **98**, 373–381 (1993).
48. E. A. Lima, B. P. Weiss, Ultra-high sensitivity moment magnetometry of geological samples using magnetic microscopy. *Geochem. Geophys. Geosyst.* **17**, 3754–3774 (2016).
49. J. L. Kirschvink, The least-squares line and plane and the analysis of palaeomagnetic data. *Geophys. J. R. Astr. Soc.* **62**, 699–718 (1980).
50. L. Tauxe, H. Staudigel, Strength of the geomagnetic field in the Cretaceous Normal Superchron: New data from submarine basaltic glass of the Troodos Ophiolite. *Geochem. Geophys. Geosyst.* **5**, Q02H06 (2004).

51. R. J. Smith, Use and misuse of the reduced major axis for line-fitting. *Am. J. Phys. Anthropol.* **140**, 476–486 (2009).
52. J. T. Armstrong, CITZAF: A package of correction programs for the quantitative electron microbeam X-ray analysis of thick polished materials, thin films, and particles. *Microbeam Anal.* **4**, 177–200 (1995).
53. R. R. Fu, E. A. Lima, M. W. R. Volk, R. Trubko, High sensitivity moment magnetometry with the quantum diamond microscope. *Geochem. Geophys. Geosyst.*, **21**, e2020GC009147 (2020).
54. D. R. Glenn, R. R. Fu, P. Kehayias, D. Le Sage, E. A. Lima, B. P. Weiss, R. L. Walsworth, Micrometer-scale magnetic imaging of geological samples using a quantum diamond microscope. *Geochem. Geophys. Geosyst.* **18**, 3254–3267 (2017).
55. S. Ebert, J. Render, G. A. Brennecka, C. Burkhardt, A. Bischoff, S. Gerber, T. Kleine, Ti isotopic evidence for a non-CAI refractory component in the inner solar system. *Earth Planet. Sci. Lett.* **498**, 257–265 (2018).
56. J. M. Schneider, C. Burkhardt, Y. Marrocchi, G. A. Brennecka, T. Kleine, Early evolution of the solar accretion disk inferred from Cr-Ti-O isotopes in individual chondrules. *Earth Planet. Sci. Lett.* **551**, 116585 (2020).
57. F. E. DeMeo, B. Carry, Solar system evolution from compositional mapping of the asteroid belt. *Nature* **505**, 629–634 (2014).
58. A. Morbidelli, K. J. Walsh, D. P. O'Brien, D. A. Minton, W. F. Bottke, in *Asteroids IV*, P. Michel, F. E. DeMeo, W. F. Bottke, Eds. (University of Arizona, 2015), pp. 493–507.
59. S. Sutton, C.M.O.'D. Alexander, A. Bryant, A. Lanzirotti, M. Newville, E. A. Cloutis, The bulk valence state of Fe and the origin of water in chondrites. *Geochim. Cosmochim. Acta* **211**, 115–132 (2017).
60. L. Testi, T. Birnstiel, L. Ricci, S. Andrews, J. Blum, J. Carpenter, C. Dominik, A. Isella, A. Natta, J. P. Williams, D. J. Wilner, in *Protostars and Planets VI*, H. Beuther, R. S. Klessen, C. P. Dullemond, T. K. Henning, Eds. (University of Arizona Press, 2014), pp. 339–361.
61. S. J. Desch, A. Kalyaan, C. M. O.'D. Alexander, The effect of Jupiter's formation on the distribution of refractory elements and inclusions in meteorites. *Astrophys. J. Suppl. S.* **238**, 11 (2018).
62. P. A. Selkin, J. S. Gee, L. Tauxe, W. P. Meurer, A. J. Newell, The effect of remanence anisotropy on paleointensity estimates: A case study from the Archean Stillwater Complex. *Earth Planet. Sci. Lett.* **183**, 403–416 (2000).

63. G. Siron, K. Fukuda, M. Kimura, N. T. Kita, New constraints from ^{26}Al-^{26}Mg chronology of anorthite bearing chondrules in unequilibrated ordinary chondrites. *Geochim. Cosmochim. Acta* **293**, 103–126 (2021).
64. G. Siron, N. T. Kita, K. Fukuda, M. Kimura, in *Lunar and Planetary Science Conference* (2021), p. 1639.
65. A. T. Hertwig, M. Kimura, T. Ushikubo, C. Defouilloy, N. T. Kita, The ^{26}Al-^{26}Mg systematics of FeO-rich chondrules from Acfer 094: Two chondrule generations distinct in age and oxygen isotope ratios. *Geochim. Cosmochim. Acta* **253**, 111–126 (2019).
66. K. Nagashima, A. N. Krot, M. Komatsu, ^{26}Al–^{26}Mg systematics in chondrules from Kaba and Yamato 980145 CV3 carbonaceous chondrites. *Geochim. Cosmochim. Acta* **201**, 303–319 (2017).